RSC Applied Interfaces

REVIEW

View Article Online
View Journal | View Issue

Cite this: *RSC Appl. Interfaces*, 2024, **1**, 11

Nanoporous oxide electrodes for energy conversion and storage devices

Jin Wook Yang,†[a] Hee Ryeong Kwon,†[a] Jin Ho Seo,†[a] Sangwoo Ryu*[b] and Ho Won Jang *[ac]

Nanoporous oxides have been established as key materials for constructing electrodes for energy conversion and storage devices, offering high surface area and a large number of active sites for electrochemical reactions. Herein, we mainly focus on the characteristics, synthesis, and application of various nanoporous oxide electrodes for energy conversion and storage devices. Features of various nanoporous oxides by dimensionality and their functionalities in electrodes are presented. The synthesis strategies for nanoporous oxide electrodes to control their morphology are introduced, including top-down and bottom-up methods. Recent advances in nanoporous oxide electrodes in energy conversion and storage devices, such as fuel cells, water splitting electrodes, solar cells, light-emitting diodes, batteries, and supercapacitors, are summarized. The roles of nanoporous oxides tailored to the specific requirement for high performance of each device are further discussed. This review provides valuable insights into the design of nanoporous oxide electrodes from a materials point of view, contributing to renewable energy technologies.

Received 29th June 2023,
Accepted 30th August 2023

DOI: 10.1039/d3lf00094j

rsc.li/RSCApplInter

1. Introduction

Nanoporous oxides have gained significant attention as highly promising materials in the field of energy conversion and storage, revolutionizing the landscape of renewable energy technologies. With their tailored porosity and high surface area, nanoporous oxide electrodes offer unique structural and functional properties, enabling enhanced performance and efficiency in applications such as fuel cells, solar cells, batteries, supercapacitors, *etc.*[1–4] As a result, various research studies have focused on the synthesis, characterization, and application of nanoporous oxide materials.

The distinctive features of nanoporous oxide electrodes stem from their high surface area and ability to provide a large number of active sites for reactions, facilitating efficient

[a] *Department of Materials Science and Engineering, Research Institute of Advanced Materials, Seoul National University, Seoul 08826, Republic of Korea. E-mail: hwjang@snu.ac.kr*
[b] *Department of Advanced Materials Engineering, Kyonggi University, Suwon 16227, Republic of Korea. E-mail: sryu@kyonggi.ac.kr*
[c] *Advanced Institute of Convergence Technology, Seoul National University, Suwon 16229, Republic of Korea*
† These authors contributed equally to this work.

Jin Wook Yang

Jin Wook Yang received his Ph.D. from the Department of Materials Science and Engineering at Seoul National University in 2023. He is currently working as a postdoc fellow under the supervision of Prof. Ho Won Jang. His research interests include materials synthesis and designing (photo) electrocatalysts for energy conversion devices.

Hee Ryeong Kwon

Hee Ryeong Kwon is currently a Ph.D. candidate under the supervision of Prof. Ho Won Jang at the Department of Materials Science and Engineering of Seoul National University. She received her B.S. degree from the Department of Materials Science and Engineering at Korea University in 2021. Her current research focuses on the synthesis and design of photoelectrochemical energy conversion devices.

charge transfer and ion diffusion processes. In electrochemical devices, the controlled porosity provides abundant active sites for electrochemical reactions and electrolyte penetration, improving stability in terms of accommodating volume changes upon oxidation–reduction reactions.[5–7] Also, in energy conversion devices related to light energy, such as water splitting electrodes, solar cells, and light-emitting diodes (LEDs), complex nanostructures are advantageous for confining or emitting light, contributing to the high efficiency of devices.[8–10]

This review aims to provide a systematic overview of the recent advancements in nanoporous oxide electrodes for energy conversion and storage devices. First, we introduce nanoporous oxides by dimensionality and explain examples and characteristics of each structure. Then, we describe the advantages of nanoporous oxides in terms of charge and ion transport, light management, and active sites. Additionally, we delve into the various synthesis strategies employed to fabricate nanoporous oxide materials with precise control over their pore size, morphology, and composition. Furthermore, we explore the applications of nanoporous oxide electrodes in diverse energy conversion and storage devices. We highlight the performance enhancements achieved through the integration of nanoporous oxide electrodes and the key factors influencing their performance. Finally, we address the challenges and future perspectives in the field of nanoporous oxide electrodes. This covers strategies for improving their stability, scalability, and cost-effectiveness and expanding their applications in emerging energy technologies. By providing a comprehensive review of nanoporous oxide electrodes for energy conversion and storage devices, their potential expands the landscape of sustainable energy systems.

2. Nanoporous oxides

2.1. Structural features

Nanoporous oxides feature unique structures and properties by taking a porous structure and downsizing it to the nanoscale. These oxides possess a network of interconnected pores or voids with dimensions typically ranging from a few nanometers to a few hundred nanometers. Representative structures of nanoporous oxides can be classified into two categories. Firstly, some nanoporous oxides inherently possess internal pores within their substance.[11] According to the International Union of Pure and Applied Chemistry (IUPAC) classification system, the common classification of porous materials is based on their pore sizes, which divides porous materials into microporous (with pore diameters of <2 nm), mesoporous (2–50 nm), and microporous (>50 nm) categories.[12] These different-sized pores can be arranged either randomly or in an orderly manner to create numerous

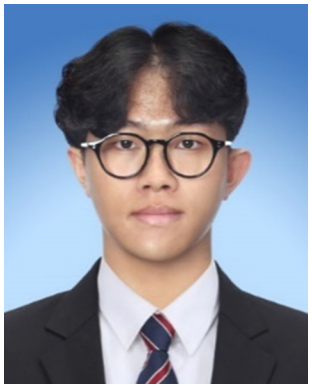

Jin Ho Seo

Jin Ho Seo is currently a Ph.D. candidate under the supervision of Prof. Ho Won Jang at the Department of Materials Science and Engineering of Seoul National University. He received his B.S. degree from the Department of Materials Science and Engineering at the University of Seoul in 2023. His current research interests include materials synthesis and designing high entropy alloy materials for energy conversion devices.

Sangwoo Ryu

Sangwoo Ryu is an assistant professor at the Department of Advanced Materials Engineering of Kyonggi University. He received his Ph.D from the Department of Materials Science and Engineering at Pohang University of Science and Technology in 2010. He worked as a research associate at the University of Wisconsin-Madison from 2010 to 2016, and he worked as a research professor at KAIST from 2016 to 2018 before he joined Kyonggi University in 2018. His research interests are nanostructured (photo)electrochemical catalysts for hydrogen production and CO_2 reduction, chemical and biosensors, and various ceramic thin film heterostructures.

Ho Won Jang

Ho Won Jang is a full professor at the Department of Materials Science and Engineering of Seoul National University. He received his Ph.D. from the Department of Materials Science and Engineering at Pohang University of Science and Technology in 2004. He worked as a research associate at the University of Wisconsin-Madison from 2006 to 2009. Before he joined Seoul National University in 2012, he had worked at the Korea Institute of Science and Technology (KIST) as a senior research scientist. His research interests include materials synthesis and device fabrication for (photo)electrocatalysis, chemical sensors, memristors, micro-LEDs, and thin film transistors.

oxide structures with a high surface area. Secondly, nanoporous oxides also include structures with pores formed within the volume space of matrices due to nanostructured architectures, which encompass a wider range.[13] These nanostructured oxides can exhibit various morphologies, such as nanoparticles,[14] nanowires,[15] nanotubes,[16] or nanosheets.[17] Furthermore, they can be diversified into distinct nanostructures that are advantageous in increasing the surface-to-volume ratio and accelerating the transport routes of mediators such as charge and light. In this review, we will cover numerous cases of nanoporous oxides by combining all the categories.

In oxide materials, oxygen bonding plays a crucial role in forming strong bonds with other elements, leading to the formation of stable oxide structures. The specific bonding arrangements between metal and oxygen atoms determine the properties such as electrical conductivity, magnetic and optical behaviors, and catalytic properties.[18] For example, basically, binary metal oxides include titania (TiO_2),[19] silica (SiO_2),[20,21] alumina (Al_2O_3), *etc.*[22] Ternary oxides are exemplified by perovskite structures[23] and intercalation compounds,[24] and multinary oxides exist in various compositions. Besides that, graphene oxide (GO), a derivative of graphene, is a form of oxide material with oxygen functional groups attached to sp^2 hybridized carbon atoms and the carbon lattice.[25] By incorporating nanoporous structural strategies, these oxides with compositional diversity can be utilized as more effective electrodes for energy conversion and storage. As shown in Fig. 1, there are various nanoporous architectures that oxide materials can take, from zero-dimensional (0D) to three-dimensional (3D) structures. In this chapter, the structural characteristics of nanoporous oxides will be focused extensively on each dimensionality of the materials. In addition, we will discuss the strengths of nanoporous oxides, which play a major role in energy conversion and storage materials.

2.2. Dimensionality

2.2.1. Zero-dimensional (0D) oxides. Zero-dimensional (0D) oxides are characterized by sub-nanometer-sized particles that are confined in all dimensions, such as nanoparticles,[26] quantum dots,[27] and clusters.[28] The confined dimensions of 0D oxides give exceptional properties, including high specific surface area and rapid charge carrier transport. Due to their small size, these structures also exhibit quantum confinement effects, where the electronic and optical properties differ from their bulk counterparts.[27] This confinement leads to size-dependent properties such as enhanced electrical conductivity, optical absorption, and mechanical strength. The ability to precisely control the size and morphology of 0D oxides offers tremendous potential for advanced nanomaterials in specific applications. We will examine the advances in 0D oxides that have experienced various composition and structural alterations.

Essentially, since the particle size and the surface area of each particle are inversely proportional, synthesis techniques for smaller-sized solid nanoparticles have been developed. As mechanistic studies on the synthesis principle of solid-state or liquid-phase chemistry are supported, oxides with various compositions and precisely controlled sizes are inexhaustible.[29] Among them, wide band gap semiconductor metal oxides, including ZnO,[30] TiO_2,[31] SnO_2,[32] and NiO,[33] have been studied with their unique advantages. Among the intense development efforts, Chen *et al.* succeeded in synthesizing black TiO_2 nanocrystals through hydrogenation, broadening solar absorption for photocatalysis.[34] The hydrogenated-black TiO_2 nanocrystals were about 8 nm in diameter with a disordered outer layer surrounding a crystalline core of 1 nm thickness (Fig. 2a). This structural analysis, which discovered the lattice disorder of particles at the nanoscale, demonstrated that TiO_2 nanoparticles' extended energy states enhance light absorption. In a recent study, a synthesis method has been proposed for TiO_2 and antimony-doped tin oxide (ATO), utilizing calcination to achieve higher crystallinity while concurrently preventing the formation of nanoparticle agglomerates without sacrificial materials.[35] This synthesis approach can be extended to a broader range of oxide materials, allowing for the formation of stable colloidal solutions with tailored crystallinity. On the other hand, in smaller 1.6 nm size WO_x nanoparticles, the quantum confinement effect was confirmed in a limited width as the nanocrystal size became smaller.[36] WO_x quantum dots synthesized through the colloid process were identified to have excellent crystallinity and ultra-small crystal size through high-resolution transmission electron microscopy (HRTEM) images. Downsizing to 0D showed faster electrochemical kinetics compared to bulk materials, along with an increase in the band gap due to the strong quantum confinement. Metal oxide nanoparticles with narrower band gaps, such as Fe_2O_3 (ref. 37) and $BiVO_4$,[38] also

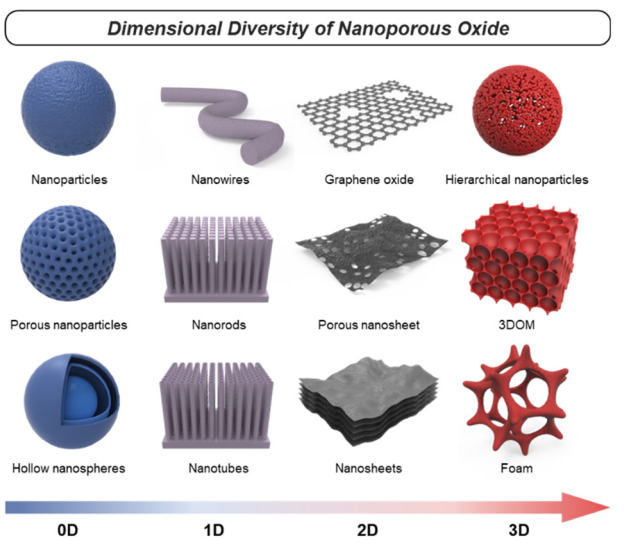

Fig. 1 Schematics of various nanoporous oxides.

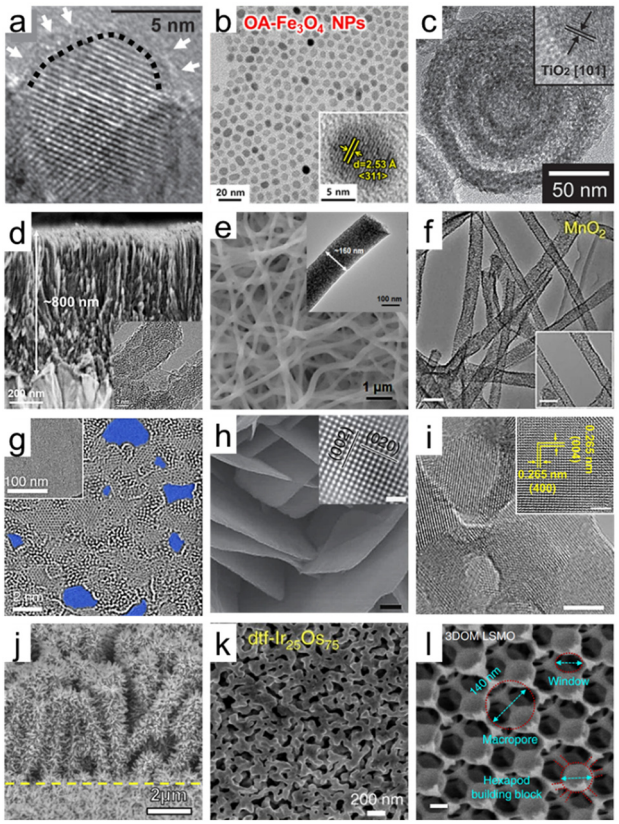

Fig. 2 Dimensional diversity in the structure of porous oxide materials. (a) HRTEM image of hydrogenated TiO_2 nanocrystals. A short dashed curve is applied to outline a portion of the interface between the crystalline core and the disordered outer layer. Reproduced from ref. 34. Copyright 2011 AAAS. (b) HRTEM images of Fe_3O_4 nanoparticles. The inset indicates the lattice fringe spacing. Reproduced from ref. 40. Copyright 2023 Elsevier. (c) HRTEM images of multi-shell hollow TiO_2 nanoparticles. Reproduced from ref. 44. Copyright 2014 Wiley. (d) Cross-sectional SEM image of ultrathin corrugated TiO_2 nanowire arrays. The inset indicates the HRTEM image of ultrathin corrugated TiO_2 nanowire arrays. Reproduced from ref. 55. Copyright 2022 American Chemical Society. (e) SEM image of high entropy oxide nanofibers. The inset indicates the HRTEM image of high entropy oxide nanofibers. Reproduced from ref. 57. Copyright 2022 Wiley. (f) TEM images of MnO_2 nanotubes (scale bar: 100 nm). Reproduced from ref. 59. Copyright 2015 Springer Nature. (g) HRTEM images of graphene oxide (GO) sheets after being etched for 1 h. Pores are highlighted in blue color. Reproduced from ref. 65. Copyright 2019 Springer Nature. (h) SEM image of WO_3 nanosheets (scale bar: 200 nm). The inset indicates the HRTEM image of the crystal lattice structure of WO_3 nanosheets (scale bar: 1 nm). Reproduced from ref. 70. Copyright 2014 Springer Nature. (i) TEM images of Y_2O_3 porous nanosheets (scale bars: 5 nm). The inset indicates the HRTEM image of the crystal lattice structure of Y_2O_3 nanosheets (scale bar: 2 nm). Reproduced from ref. 72. Copyright 2022 AAAS. (j) SEM image of CuO/ZnO nanorods. Reproduced from ref. 80. Copyright 2016 Elsevier. (k) SEM image of Ir/IrO_2 of dealloyed $Ir_{25}Os_{75}$. Reproduced from ref. 86. Copyright 2017 Springer Nature. (l) SEM image of 3DOM $La_{0.6}Sr_{0.4}MnO_3$ (LSMO) (scale bars: 200 nm). Reproduced from ref. 95. Copyright 2017 Springer Nature.

make use of functions derived from the nanoscale geometry. Additionally, in spinel crystal structured-oxides with pseudocapacitive characteristics, a liquid-phase reaction synthesis has been devised.[39] This synthesis enables sophisticated size control of MFe_2O_4 (M = Fe, Co, Mn, *etc.*) nanoparticles in the range of 3 to 20 nm. Based on the previous research, Ahn *et al.* synthesized monodispersed nanoparticles of Fe_3O_4 and conductive indium tin oxide (ITO) and applied them to pseudocapacitor electrodes.[40] Fig. 2b shows the high crystallinity of Fe_3O_4 nanoparticles and the uniformly controlled spherical size. Various oxides, such as those mentioned, have been investigated in the form of nanoparticles. Note that this research extends beyond simple geometric properties, aiming to achieve changes in electronic and optical characteristics as valuable energy materials. By modifying the electronic structure and controlling the crystalline properties, their impact has been significantly amplified.

Starting from solid nanospheres, nanoporous 0D materials can take on various structural modifications, transforming into hollow nanoparticles with empty interiors and core–shell or yolk–shell structures.[41] Advances in nanotechnology have made it possible to precisely control the porosity, thickness, and number of shells and core and yolk materials. These advanced nanoparticles provide wide inner and outer surfaces, a fast charge transport path, and efficient light harvesting by multiple scattering. A study on Fe_2O_3 nanoparticles proved the advantage of the hollow shape by directly comparing solid and hollow nanoparticles with the performance of Li-ion batteries. The process of obtaining a hollow structure not only provides a larger reactive surface area on both sides but also leads to the formation of more cation vacancies, resulting in higher intercalation and conversion capacities.[42] Specifically, the nanoporous geometry of hollow nanoparticles can be analyzed by N_2 sorption isotherms based on the Brunauer–Emmett–Teller (BET) method, showing an increase in the BET surface area with decreasing shell thickness of hollow nanoparticles.[43] As shown in Fig. 2c, the number of shells can be increased, and Hwang *et al.* introduced multi-shell TiO_2 hollow nanoparticles with three shells to maximize the effect of multireflection.[44] The synthesized multi-shell TiO_2 hollow nanoparticles had a BET surface area of 171.3 $m^2\ g^{-1}$, which is 2.7 times higher than the 63.6 $m^2\ g^{-1}$ of the single shell. In addition, nanoporous characteristics were maximized with pores with a diameter of 4.09 nm in the shells themselves. Furthermore, oxide nanoparticles have been increasingly engineered into more complex structures for specific applications. Core–shell or yolk–shell oxide nanoparticles can also be formed with other materials, such as metals and organics.[45,46] The structure of a porous CeO_2 shell on a monometallic Pt yolk or bimetallic PtAg yolk is an example of an elaborate hetero-nanostructured oxide design.[47] The yolk–shell structure allows for the encapsulation of different materials within the core, enabling the design of multifunctional nanoparticles with controlled release properties. Designing 0D structures with greater intricacy demonstrates the ongoing evolution of customized functionality. Therefore, it becomes evident that tailored

interfaces using diverse oxides to harness the physicochemical properties can alter characteristics such as conductivity, catalytic activity, or optical behavior. Anticipating the synergy among individual components, the development of complex 0D nanoporous oxides becomes necessary.

2.2.2. One-dimensional (1D) oxides. One-dimensional (1D) nanoporous oxides feature high aspect ratio nanostructures, having one dimension much larger than the other two. These structures have a highly porous nature, with a network of interconnected pores or channels running along their length. Individual 1D structures combine to form a nanoarray, and the formation of numerous open spaces between neighboring 1D nanostructures also contributes to the porous properties. The most common types of one-dimensional porous nanostructures include nanowires, nanorods, and nanotubes.[48] Additionally, there are more diverse structures such as nanoneedles,[49] nanobelts,[50] and nanoribbons.[51] These structures, taking advantage of both 1D architectures and nanoporosity, have been extensively applied in fields where a large surface area and fast ionic and electronic transport kinetics are essential.[52]

When we delve into more specific examples of synthesized 1D structures, a prominent case is TiO_2 1D semiconductors, which have made significant progress in the fields of photocatalysis and dye-sensitized solar cells (DSSCs).[53] As the understanding of solution-based synthesis has improved, it has become possible to finely tune the length, diameter, and density of TiO_2 nanorods or nanowires with specific crystal orientations and phases. Xing *et al.* synthesized well-separated single-crystal rutile TiO_2 nanowire arrays with a length of 9 μm by a solvothermal method.[54] The straight axial 1D geometry not only serves as an excellent charge separation and transport channel on its own but also provides a wide surface area, enabling effective noble metal decoration. Recently, the mono-micelle-directed assembly method has enabled the precise arrangement of extremely thin nanowires in TiO_2 nanowire arrays (Fig. 2d).[55] These nanoarrays consist of nanowires with a diameter of 8 nm, vertically aligned in a uniform spacing of 8 nm. Moreover, there are tightly packed concave structures with a diameter of 5 nm along the nanowire axis, forming a corrugated morphology. This design exploits the advantages of a nanoporous structure in a 1D configuration by reducing the radial distance and creating a direct axial pathway. In addition, other metal oxides such as SnO_2, ZnO, Fe_2O_3, CuO, and Cu_2O have been successfully synthesized in 1D nanoporous structures to obtain enhanced functionalities compared to their flat film structures. For the perovskite oxide materials, pioneering work by Hildebrandt *et al.* demonstrated the successful application of electrospinning to synthesize nanofibers of perovskite oxide materials, specifically $Ba_5Ta_4O_{15}$ with its (111)-layered structure.[56] In the synthesis process of $Ba_5Ta_4O_{15}$ nanofibers, the $BaCO_3$ intermediate stabilized and strengthened the fiber 1D morphology during polymer decomposition, providing high crystallinity with a length of several micrometers. Furthermore, it is possible to achieve 1D nanofibers of high entropy oxides, which are multicomponent oxides homogeneously mixed in a single crystal phase with five or more cation elements. The scanning electron microscopy (SEM) and transmission electron microscopy (TEM) images in Fig. 2e present $(Mg_{0.2}Mn_{0.2}Co_{0.2}Ni_{0.2}Zn_{0.2})Fe_2O_4$ nanofibers with tens of micrometers in length and a diameter of 160 nm having abundant nanocrystals.[57] As a result of N_2 adsorption and desorption isotherm analysis, the synthesized high entropy nanofibers had a large specific surface area of 384.4 $m^2\ g^{-1}$. The synergistic effect of multiple metal compositions and the 1D nanoporous structure leads to enhanced chemical adsorption abilities, making it a promising approach for various catalytic applications.

Nanotubes, on the other hand, are hollow cylindrical structures with nanoscale diameters. Anodizing metal foil is one of the representative methods to obtain metal oxide nanotube arrays. Geometrical modifications such as nano-bamboo and double-walled nanotubes can be achieved by controlling the anodization parameters.[58] Another typical method is to obtain nanotube fibers through the calcination of nanofibers obtained by electrospinning. Niu *et al.* have developed an effective method for nanotube synthesis that can be applied to various materials, including inorganic single-metal oxides, binary-metal oxides, and multi-element oxides.[59] An important mechanism to obtain porous oxide nanotubes in the electrospinning and pyrolysis processes is to set the gradient distribution of poly(vinyl alcohol) (PVA) while varying the molecular weight. Fig. 2f shows the synthesized MnO_2 nanotubes with a diameter of approximately 50 nm. These nanotubes also exhibit abundant mesopores on their tube walls, ensuring a significantly enhanced specific surface area compared to nanowires. Besides, the electrospinning method, along with different post-treatments, has been applied to synthesize some interesting nanoporous 1D structures.[60] For instance, a tube-in-tube structured spinel oxide including $CoMn_2O_4$, $NiCo_2O_4$, $CoFe_2O_4$, $NiMn_2O_4$, and $ZnMn_2O_4$ can be made into a 1D nanoporous structure by controlling the heating rate. In comparison to nanotubes and solid nanofibers, which have BET surface areas of 28.0 and 12.9 $m^2\ g^{-1}$, the resulting spinel oxide nanotubes exhibit a significantly higher BET surface area of 47.3 $m^2\ g^{-1}$.[61] By carefully designing the fabrication process and parameters, researchers can tailor the size, morphology, and surface chemistry of the nanopores, allowing for precise control over the physicochemical properties. On the other hand, in terms of material development, it's essential to maintain structural stability while harnessing the advantages of 1D structures. The ultimate goal is to engineer materials with porous structures and desired properties under various challenging conditions, enabling successful applications across a wide range of industries. Therefore, understanding how stresses affect structural stability and developing solutions to enhance the robustness are also key aspects of 1D oxide development.

2.2.3. Two-dimensional (2D) oxides. Two-dimensional (2D) oxides are arranged in a lateral plane with a thickness ranging from a few to tens of nanometers. Due to their ultrathin structure, 2D nanoporous oxides have an extremely high surface-to-volume ratio even compared with 0D and 1D low-dimensional materials. In the lateral plane, 2D structures provide an oriented charge transport pathway and reduce electrical resistance. At the edge sites of the plane, unique atomic arrangements can lead to increased reactivity, changes in the electronic structure, and the introduction of new functionalities.[62] Additionally, 2D oxide materials exhibit remarkable flexibility and mechanical strength attributed to the atom-level thickness and strong in-plane covalent bond, and fascinating optical properties due to quantum confinement effects. Recently, various 2D nanoporous oxides have been actively explored to make use of these inherent advantages. The structure of 2D oxides ranges from nanosheets and nanoplates to a single monolayer, and each nanoporous 2D oxide structure will be discussed in this section.

In 2D oxides, layered crystal oxides and non-layered crystal oxides are two different structural arrangements.[63] Layered crystal oxides, also known as lamellar oxides, have a layered structure in which the oxygen atoms are arranged in stacked planes. The layers can be considered 2D sheets, and they are held together by weak van der Waals forces or other weak interlayer interactions. Examples of layered crystal oxides include graphite oxide, MnO_2, V_2O_5, MoO_3, and WO_3. These layered oxides can be delaminated into 2D monolayer nanosheets *via* top-down exfoliation methods, including mechanical force exfoliation, mild chemical exfoliation, and electrochemical exfoliation. Intriguingly, GO, which has universal applicability in energy conversion and storage fields due to its unique functionality, is derived from a monolayer of graphite oxide.[64] Fig. 2g demonstrates the formation of sub-nanometer nanopores in a single layer of GO, indicating that the nanoporosity of GO can be increased through oxidative etching.[65] In addition, GO nanosheets with a narrow pore size distribution centered around 0.4 nm and a high BET surface area of 611 m^2 g^{-1} have been synthesized through calcination. The nanoporous GO electrodes have the benefits of abundant active sites based on their large surface area and nanopores in electrocatalytic reactions.[66] For layered metal oxide 2D nanosheets, Yang *et al.* reported 2D MnO_2 nanosheets intercalated with alkali metal cations by electrochemically exfoliating from bulk Mn metal. The synthesized nanosheets successfully achieved a mesoporous 2D geometry with pore sizes of 3–4 nm. In non-layered oxides, on the other hand, all atoms are linked by strong chemical bonds, leading to high-energy surfaces with surface dangling bonds. Some examples of non-layered oxides include WO_3, TiO_2, SnO_2, and ZnO. Non-layered oxides without anisotropy make their exfoliation challenging, but a comprehensive knowledge of the surface energy and atomic bonding within the crystal structure has recently resulted in the successful synthesis of these materials with exfoliation.[67,68] An example of such cases involves the synthesis of 2D nanocrystals with a thickness of 2 nm by insertion of K into bulk non-layered structures of wurtzite ZnO, β-MnO_2, and anatase TiO_2 through heat reaction under vacuum conditions.[69]

Nevertheless, the top-down approach has limitations in application depending on the crystal structure, low controllability, and low yield. As an alternative, a bottom-up synthesis has also been developed which can be applied more universally regardless of the crystal structure. More generalized bottom-up techniques have been investigated extensively in this flow, and one of them is the surfactant self-assembly method. This synthesis process includes forming inverse lamellar micelles using surfactants, incorporating hydrated inorganic oligomers, and subjecting them to hydrothermal or solvothermal treatment for improved organization and crystallization, resulting in well-crystallized nanosheets. It has been effectively used for certain transition metal oxides, including TiO_2, ZnO, Co_3O_4, WO_3, Fe_3O_4, and MnO_2. The final product applied to WO_3 exhibits a well-defined 2D nanosheet morphology with high crystallinity, as observed in the SEM and HRTEM images (Fig. 2h).[70] Following such pioneering research, there has been active progress in the development of methods using 2D sacrificial templates and *in situ* analysis to elucidate the synthesis mechanism of 2D structured oxides.[65,71] Yang *et al.* observed the 3D-to-2D transformation in rock salt structured cobalt oxide using *in situ* liquid-phase TEM. They revealed that the driving force of dimensional change is the variation in surface energy during the growth process, as supported by density functional theory calculations.[65] In a recent study, a universally applicable synthesis method for nanoporous oxide nanosheets has been presented, which can be extended to rare-earth oxides, transition metal oxides, III-group metal oxides, II-group metal oxides, composite perovskite oxides, and high entropy oxides. The reported technique is a relatively simple and cost-efficient approach, utilizing a carbon template formed through the Maillard reaction of ammonium nitrate and glucose, along with a puffing process. The application of Y_2O_3 is shown in Fig. 2i, which reveals a dense arrangement of nanopores and an ultrathin 2D structure, highlighting its high surface area and excellent crystallinity.[72] As such, new insights into the 2D oxide materials are being provided, and with adjustable porosity and structural stability, they are expected to be widely utilized in the field of energy nanotechnology.

2.2.4. Three-dimensional (3D) oxides. Three-dimensional (3D) oxides refer to nanostructures that possess three dimensions: length, width, and height. 3D nanoporous oxides can be represented as hierarchical structures that possess nanoporous hierarchy over different lengths based on an arrangement of pores, channels, and multi-level networks of interconnected voids. By integrating a diverse combination of 0D to 2D low-dimensional oxide nanostructures as the basic building units, structural diversity has been achieved. As examples of structures, there

are branched nanorods and nanotubes,[73] nanoflowers,[74] and nano-urchins[75] that resemble natural structures. These 3D complex structures exhibit multiple functionalities across various oxide materials. Notably, 3D nanoporosity serves as an efficient scaffold for charge transport, a buffer with minimal volume change, effective antireflective surfaces, and significantly shortened ion diffusion pathways. This section explores the structural diversity of 3D hierarchies to harness their advantages.

In the construction of the nanoporous 3D oxides, the previously discussed 0D to 2D low-dimensional nanostructures serve as both the basic framework and building components. Branched oxide nanostructures with a tree-like structure, where nanorod branches are densely attached to nanorod trunks, effectively enhance nanoporosity. Identification of the growth mechanism and advances in synthesis technology have made it possible to synthesize structurally more complex hyperbranched nanoarrays.[76] This design strategy has been widely reported with applications to various materials such as WO_3,[77] ZnO,[78] and β-MnO_2/α-Fe_2O_3,[79] through controlling the length of the constituent units of branched oxides. For example, researchers introduced hierarchical ZnO/CuO electrodes. As shown in Fig. 2j, ZnO nanorod branches uniformly grow along the entire length of CuO nanorod arrays.[80] Furthermore, hierarchical structures can be built by numerous assemblies with combinations of backbones and branches of lower-order materials. Ouyang *et al.* synthesized two types of hierarchical structure electrodes of $NiCo_2O_4$@NiO by growing ultrathin NiO nanosheets on 1D nanowires and 2D nanosheets of $NiCo_2O_4$, respectively.[81] The BET analysis results to evaluate the nanoporous structure of the two types showed that the surface area of 1D nanowires $NiCo_2O_4$@NiO is higher at 81.3 $m^2\ g^{-1}$ compared to 68.1 $m^2\ g^{-1}$ when anchored on 2D nanosheets. In another study, $LaNiO_3$@NiO nanoflowers were formed using a core–shell structure, where NiO nanosheets were wrapped around 0D $LaNiO_3$ nanoparticles.[82] Meanwhile, synthesis methods for 3D hierarchical structures have also been developed through the self-assembly of low-dimensional subunits.[83] By controlling the additives in a hydrothermal synthesis process, different crystalline nuclei were formed, resulting in diverse hierarchical morphologies such as flowers, urchins, sheet-assembled spheres, and pyramid-assembled spheres.[84] Jing *et al.* reported Bi_2MoO_6 microflowers consisting of extremely thin monolayers with a thickness of 0.8 nm.[85] The utilization of hydrophobic chains in cetyltrimethylammonium ion additives allowed for the formation of a porous hierarchical structure to reduce surface free energy rather than a stacked monolayer.

3D hierarchical oxides can take the form of a foam or sponge providing rich 3D interconnected pore networks with a porous oxide framework. A typical example is a nanoporous structure composed of an Ir core and an IrO_2 shell by dealloying of $Ir_{25}Os_{75}$ alloy as shown in Fig. 2k. Electrochemically active surface area (ECSA) tests validated the enhanced surface area of the nanoporous Ir/IrO_2 structure as an oxygen evolution catalyst. The results showed a much higher ECSA, approximately 50 times greater than a flat surface.[86] In another approach, an aliphatic ligand-based metal–organic framework (MOF) was thermally converted, resulting in nanoporous MgO and CeO_2 with high crystallinities. The aliphatic ligand serves as a self-template to create nanopores, with their size determined by controlling the thermal conversion parameters. In the well-controlled nanoporous MgO, the BET surface area is 200 $m^2\ g^{-1}$ with a pore hierarchy comprising micropores, mesopores, and macropores. A significant portion of the total pore volume is contributed by micropores, resulting in a volume of 0.37 cc g^{-1}.[87] Recently, there have been reports of synthesizing 3D foam structures by crosslinking 1D nanotubes or 2D nanoplates to create an abundant network of nanopores. On the one hand, Yan *et al.* introduced self-standing 3D hollow nanoporous SnO_2-modified Cu_xO nanotubes for high energy density lithium-ion batteries.[88] This distinctive design ensured electrical conductivity through metallic Cu nanotubes, which were then surrounded by Cu_xO and SnO_2 layers to impart resistance to mechanical strain, resulting in an overall lamellar structure. On the other hand, through the synergistic effect of 2D nanosheets and wide accessible surface area, these 3D foam-inspired electrodes demonstrate high capacity and cyclic stability when applied to $LiNi_{0.8}Co_{0.15}Al_{0.05}O_2$ (ref. 89) and VO_2 (ref. 90) battery cathode materials. At the same time, there have been advancements in visualizing complex and disordered 3D macrostructures and quantitatively assessing them using nanoscale X-ray computed tomography. These developments have greatly contributed to enhancing our understanding of intricate nanoporous 3D oxides.[91] The recent advancement in 3D disordered structures, coupled with improved characterization techniques, will undoubtedly enhance our understanding of morphology, pore distribution, and surface chemistry. We expect that this approach will allow for more informed decision-making in electrode design and optimization. Ultimately, it is imperative that we strive for these interactive developments to better grasp and obtain feedback on the operation of electrodes in energy devices. In conjunction with highly advanced fabrication techniques, a sophisticated 3D ordered macroporous (3DOM) structure can give regularity to the network of pore arrays.[92] The fabrication of the 3DOM structure involves self-assembling organic or inorganic sacrificial templates into a face-centered cubic lattice, filling metal oxide into the arranged sphere interstitials, and removing the templates. The ability to precisely control its pore architecture, like the pore size, shape, and arrangement, combined with its large surface area and tunable properties, makes it highly attractive for use in numerous fields. The structural benefits of the 3DOM morphology, which consists of periodic walls and open nanopores, have been applied to various materials such as V_2O_3 (ref. 93) and TiO_2.[94] In Fig. 2l, an SEM image of 3DOM $La_{0.6}Sr_{0.4}MnO_3$ perovskite, 140 nm macropores are closely packed, and nano-sized channels form 2D hexagonal close-

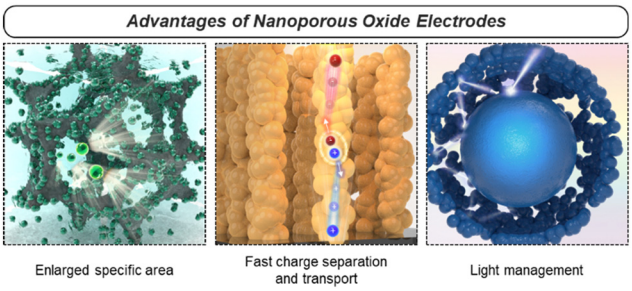

Fig. 3 Three representative advantages of nanoporous oxides.

packed arrays. The structure is also an interconnection of hexapod-like building blocks with a body diameter of 80 nm and leg lengths of 15 nm.[95] By optimizing these 3DOM architectures, it is possible to create robust and stable nanoporous structures that can withstand various environmental conditions and mechanical stresses.

2.3. Advantages

Nanoporous oxides possess various advantages that make them highly functional electrodes in energy conversion and storage applications. Specifically, nanoporous oxides provide functionalities such as enlargement of the specific surface area, fast charge separation and transport, and maximization of light utilization with their structural diversity in 0D to 3D discussed above (Fig. 3). We explore more detailed aspects of advantageous nanoporous oxides in this section.

Firstly, the enlarged specific surface area of nanoporous oxides assures an absolute exposed area where various chemical reactions can occur. In energy conversion and storage devices such as (photo)electrocatalysts, fuel cells, batteries, and supercapacitors, electrochemical reactions take place at the electrode–reactant interface. Nanoporous oxide electrodes extend an interface to interact with reactant species like ions or molecules, increasing the number of reaction sites. As a result, more reaction active sites led to higher reaction rates and improved overall performance.[96] Additionally, in energy conversion and storage systems, efficient ion transport is crucial for high-performance operation. As the surface area increases, the ion diffusion path becomes shorter, reducing transport resistance and enhancing the power density and response time of the device.[97] Aside from the major effect, the increased surface area can also contribute to high structural stability and cycling performance.[98] Nanoporous structures provide greater resistance to volumetric changes in repeated charge and discharge processes, as the free volume of their interconnected pores serves as a buffer.

Secondly, nanoporous oxide electrodes facilitate rapid charge transport by providing shorter diffusion paths with reduced resistance for the movement of charge carriers. In particular, with a quantum confinement effect and an oriented charge transport channel, low-dimensional nanoporous oxides enhance carrier mobility by reducing charge carrier scattering. In the 3DOM structure, charge carriers move along the ultrathin skeleton, thereby effectively lowering the charge transport resistance of the electrode. As in the case of devices using photo-generated charge carriers, the nanoporous geometry allows photocarriers to travel much shorter distances to the electrode–reactant interface, reducing recombination and increasing charge separation efficiency.[99] Nanoporosity can also overcome the limitation of the trade-off relationship where the depletion region and the carrier diffusion length are much shorter compared to the light penetration length in planar photoelectrodes.

Lastly, nanoporous oxides play a crucial role in increasing light absorption in solar energy conversion applications. Their rough or textured surfaces can scatter incident light multiple times, increasing the optical path length within the material. The extended path length enhances the chances of light being absorbed by the material, as it encounters more opportunities to interact with the nanostructure's surface. This light trapping effect results in a higher absorption coefficient compared to the film structure. In the fields of solar water splitting and solar cells, nanoporous photoelectrodes have been widely introduced to improve the non-directional scattering of incident light and suppress reflection.[100] The light-trapping effect in nanoporous oxide electrodes offers opportunities for improving the performance and efficiency of optoelectronic devices.

3. Synthesis of nanoporous oxides

Porosity engineering has been worth investigating, yet there are still challenging sites due to fundamental difficulties with the formation of nanoscale level pores. There are two general approaches used to synthesize nanoporous oxide materials: bottom-up and top-down methods. The conventional top-down strategy involves the use of extra energy, such as chemical, electrochemical, thermal, and mechanical processes to break down bulk materials into nano-sized structures. Top-down approaches have an imprecise surface structure yet are intrinsically straightforward to synthesize massive products. Bottom-up engineering is a method of constructing a material from atoms and molecular species. This approach has the advantage of allowing for chemical reaction-based size and shape control. In the following subsections, we will cover various synthesis techniques for preparing nanoporous oxide materials.

3.1. Bottom-up methods

The doctor blade method is one of the most utilized fabrication techniques for preparing nanoporous oxide electrodes for lithium-ion batteries,[101] DSSCs,[102–110] and electrochromic[111–113] and (photo)electrochemical performances[114–116] due to its ease of use and low price. Fig. 4a illustrates the standard doctor blade procedure for producing nanoporous oxide electrodes.[117] Before coating, the surface of the substrate is cleaned, and a solution containing particles is spread on the substrate's surface. With

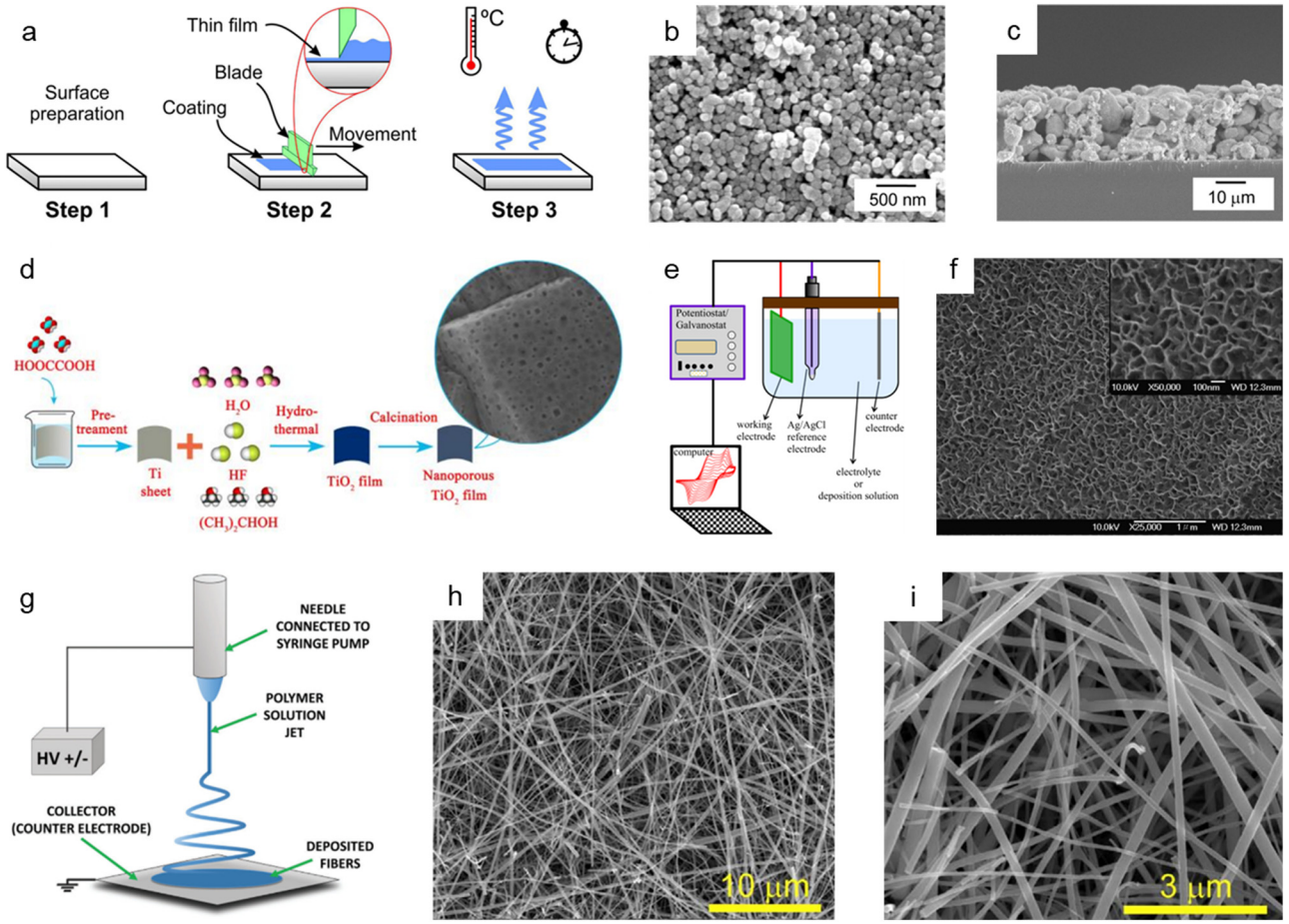

Fig. 4 Bottom-up synthesis methods of nanoporous oxides. (a) Schematic diagram showing the mechanism of the doctor blade method. Reproduced from ref. 117. Copyright 2020 Springer Nature. (b) Top view and (c) cross-sectional SEM images of the nanoporous ITO/WO_3 electrode. Reproduced from ref. 116. Copyright 2014 Elsevier. (d) A schematic illustration presenting the hydrothermal preparation of nanoporous TiO_2 films. Reproduced from ref. 129. Copyright 2015 The Royal Society of Chemistry. (e) A schematic illustration of the typical electrodeposition system. Reproduced from ref. 131. Copyright 2016 Springer Nature. (f) SEM image of the electrodeposited nickel oxide film. Reproduced from ref. 132. Copyright 2007 Elsevier. (g) Schematics of the electrospinning setup with the standard nozzle configuration where the essential parts are underlined. Reproduced from ref. 143. Copyright 2022 Wiley. (h and i) SEM images of TiO_2 nanofibers. Reproduced from ref. 149. Copyright 2017 Elsevier.

the help of a blade, the solution is evenly dispersed throughout the surface, resulting reported a nanoporous WO_3 film-coated ITO electrode prepared by the doctor-blade method for visible light-driven water splittingin a thin layer coated on the substrate. The residual solvent is then evaporated from the coated film while it is dried at the appropriate temperature to fix the coating. For example, Zhang *et al.* reported a nanoporous WO_3 film-coated ITO electrode prepared by the doctor-blade method for visible light-driven water splitting.[116] To create a nanoporous WO_3 photoanode, a solution paste made of water, WO_3 powder, polyethylene glycol, and marpolose was spread to an ITO glass surface that was cleaned with a UV-ozone treatment before being coated with a doctor blade and dried out. The final nanoporous structure on the ITO glass substrate, depicted in Fig. 4b and c, was formed by calcination at 550 °C. The synthesized nanoporous WO_3 electrode produced a photoanodic current density of 1.8 mA cm^{-2} and displayed an onset potential of 0.67 V *versus* a reversible hydrogen electrode with an incident photon to current conversion efficiency (IPCE) of 45% at a light wavelength of 400 nm and an applied potential of 1.04 V *versus* Ag/AgCl. R. Gharbi's group presented nanoporous TiO_2 for the performance of DSSCs, in which TiO_2 paste was placed on a fluorine-doped tin oxide (FTO) glass surface with the use of adhesive tape to control the thickness and offer a non-coated space for electrical contact.[107] The constructed DSSCs with nanoporous TiO_2 photoanodes demonstrated better solar-to-current energy conversion efficiency with a short-circuit current density of 0.69 mA cm^{-2}. Furthermore, Lionel Hirsch and colleagues produced nanoporous SnO_2 films for DSSCs by applying commercial SnO_2 colloidal suspensions and light-scattering SnO_2 particles over conductive substrates with 3 M Magic Tape.[109] Nanoporous SnO_2 layers revealed excellent photovoltaic responses when used as electrodes for DSSCs, with an overall power conversion efficiency of 2.27% under AM 1.5G.

The hydrothermal method has been commonly employed for synthesizing nanoporous oxides due to its simplicity, high yield, and superior crystallinity at a reasonable cost. In a typical hydrothermal approach, precursors are dissolved in an aqueous solution, sealed, and heated in a stainless steel autoclave. Without extra processing, high crystalline materials are produced by heterogeneous reactions that take place above the boiling point of water and atmospheric pressure. To successfully synthesize nanomaterials, it is essential to control the reaction parameters, such as the kind of precursor and solvent used, their concentration, stabilizing agents, reaction temperature, pressure, and duration. The reaction temperature, pressure, and time, in particular, determine the reaction rate, crystal growth, and characteristics. This method has been developed to synthesize a variety of nanoporous oxides for electrode materials that can be employed in Li-ion batteries,[118] electrochemical systems,[119–121] supercapacitors,[122–127] DSSCs,[128] and photocatalysts.[129,130] Fig. 4d depicts the fabrication process of nanoporous TiO_2 films reported by Sekiguchi's group using a hydrothermal method for photocatalytic use.[129] Before being immersed in HF aqueous solution with isopropanol in a Teflon-lined autoclave, a metallic Ti sheet was first etched with oxalic acid to remove the oxide layer. After the hydrothermal treatment, the Ti-sheet was washed with deionized water, dried in air, and then calcined at 600 °C. The as-made nanoporous TiO_2 films with exposed {001} facets displayed superior UV photocatalytic activity. Cui *et al.* described the hydrothermally produced 3D nanoporous bamboo leaf-like copper oxide with a grain size of 50–80 nm for supercapacitive performance.[125] The as-synthesized CuO electrode showed a specific capacitance of 269.6 F g^{-1} at a current density of 0.25 A g^{-1} and a capacitance retention ratio of 88.79% at a current density of 2 A g^{-1}. Additionally, Bao *et al.* prepared nanoporous zinc oxide by a single hydrothermal step for the electrochemical reduction of CO_2.[119] The nanoporous ZnO demonstrated a substantially higher CO faradaic efficiency of 92.0%, indicating that the zinc oxide's nanopores boosted the electrocatalytic reduction of CO_2.

Electrodeposition, which has the advantages of being straightforward and affordable and having increased interfacial interaction between substrates and coating materials, is another efficient technique for creating nanoporous oxide materials. The compositions, structures, and morphologies may be easily manipulated by modifying electrodeposition conditions. The conventional electrodeposition setup includes an anode, a cathode, an electrolyte solution in an electrochemical cell, and external power sources, as shown in Fig. 4e.[131] The electrolyte solutions, in which an anode and a cathode are immersed, include metallic salts dissolved in water. Metallic ions are deposited as solid metals on the substrates by the electric current generated by external power sources through the electrolyte solution. By adjusting the voltage, pulse frequency, space between the components, deposition duration, and the use of nonconductive masks, porosity can be controlled through this technique. Electrodeposition has drawn attention in different applications (*e.g.*, capacitors,[132–134] batteries,[135,136] DSSCs,[137–139] electrochemistry[133,140–142]). Fig. 4f shows the SEM images of a nickel oxide film electrodeposited onto a stainless steel substrate for electrochemical capacitors using a plating bath of sodium acetate, nickel sulfate, and sodium sulfate mixture.[132] The electrodeposition was performed in a standard three-electrode cell with an anodic current of 0.5 mA cm^{-2}, and the deposited layer became highly porous after annealing at 300 °C. The synthesized nickel oxide film demonstrated outstanding performance with a specific capacitance of 167.3 F g^{-1} at 1 A g^{-1} and 156.6 F g^{-1} at 16.5 A g^{-1} charge/discharge. Luo *et al.* prepared a nanoporous ZnO thin film produced through cathodic electrodeposition for enhanced performance in DSSCs.[139] The DSSCs made from nanoporous ZnO films achieved the highest solar-to-electric energy conversion efficiency of 5.08%, exceeding previous ZnO film-based DSSC efficiency levels. Likewise, Im *et al.* reported ultrathin nanoporous $CuCo_2O_4$ nanosheets produced *via* electrodeposition and air annealing as a bifunctional electrode for supercapacitors and water oxidation catalysis.[133] The nanoporous $CuCo_2O_4$ electrode possessed a high specific capacitance of 1473 F g^{-1} at 1 A g^{-1} and an overpotential of 260 mV at 20 mA cm^{-2} with a Tafel slope of around 64 mV dec^{-1} in 1 M KOH solution.

Electrospinning is a versatile production technique used to produce continuous nanoporous oxide fibers with diameters less than 100 nm and a variety of compositions. Fig. 4g depicts an illustration of the fundamental electrospinning system, which consists of a high-voltage system, needles, and a collector.[143] An exposed liquid droplet is electrified and subsequently extended toward the opposing collector when an electric field is generated between two electrodes. The qualities of the electrospun fibers can be adjusted using a variety of process parameters. For instance, the type of solvent or polymer used in the solution, the reaction temperature, the relative humidity, the electrical polarity applied to the nozzle, the distance between the nozzle and the collector, and the applied voltage, and all of these factors have a significant impact on the production of the final product. Molecular configurations and chemistry on the fiber's surface can be altered by changing a process parameter, which changes the fiber's properties to suit different applications, such as lithium-ion batteries,[144–148] lithium-ion storage,[149] DSSCs,[150] and supercapacitors.[145,151,152] Fig. 4h and i present the SEM images of as-grown TiO_2 nanofibers produced by two-step electrospinning for enhanced and rapid lithium-ion storage, as reported by Vilas G. Pol and co-workers.[149] After wrapping reduced graphene oxide (rGO) onto anatase TiO_2 nanofibers, the BET surface area increased from 54 m^2 g^{-1} to 105 m^2 g^{-1}, resulting in a nanoporous structure with pore sizes ranging from 5 to 20 nm. The nanofiber anodes achieved a high reversible lithium-ion storage capacity of 200 mA h g^{-1} with a

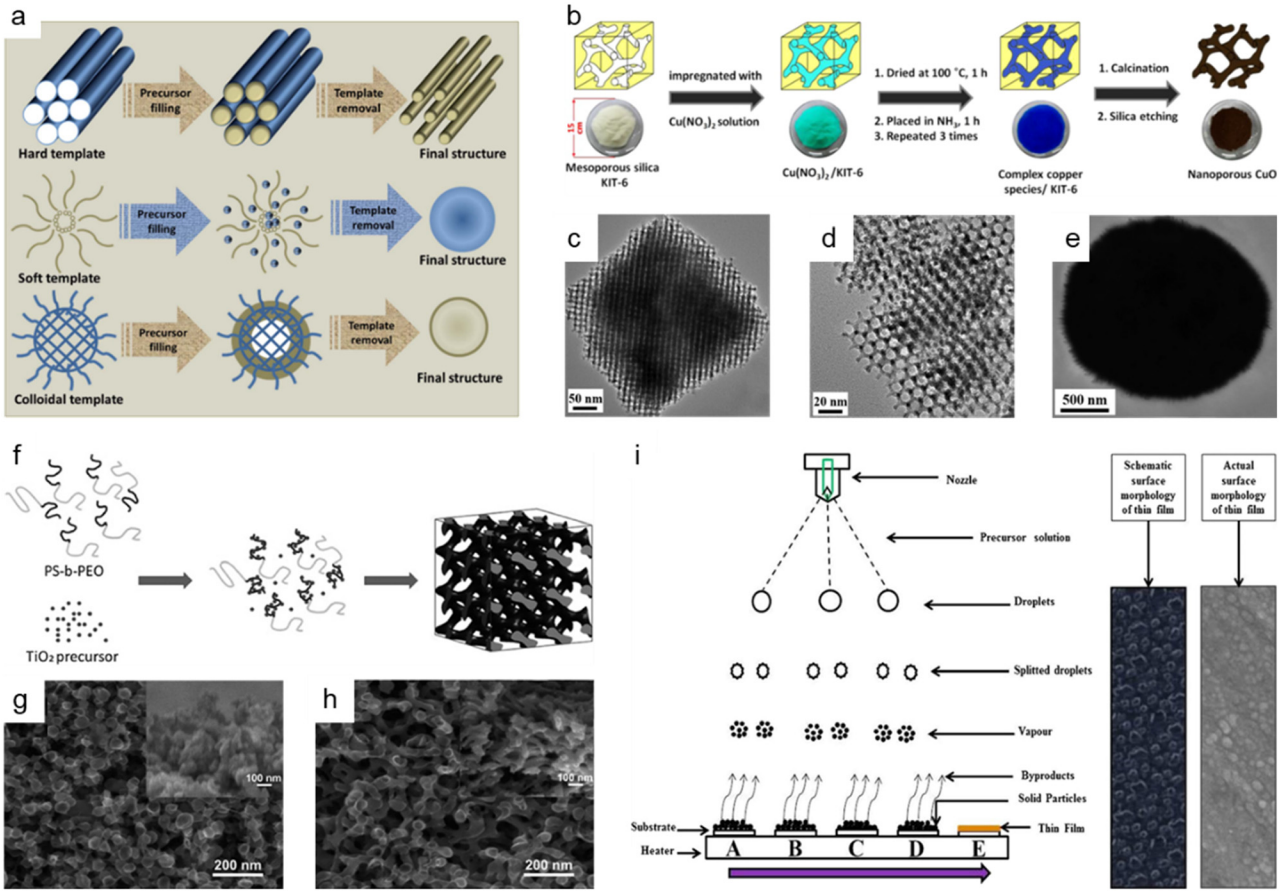

Fig. 5 Bottom-up synthesis methods of nanoporous oxides. (a) A schematic representation of the synthesis of materials using different types of templates. Reproduced from ref. 153. Copyright 2020 The Royal Society of Chemistry. (b) Schematic illustrations showing the synthesis of 3D highly ordered nanoporous CuO by nanocasting from KIT-6. (c and d) Typical TEM images of the 3D highly ordered nanoporous CuO. (e) Typical TEM images of the bulk CuO. (b–e) Reproduced from ref. 157. Copyright 2015 American Chemical Society. (f) Schematic diagram of the formation mechanism of nanostructured TiO_2 using the PS-*b*-PEO block copolymer as a template. SEM images of nanostructured TiO_2 films on FTO glass prepared with titania to polymer weight ratios of (g) 0.5 : 1 and (h) 1 : 1. (f–h) Reproduced from ref. 161. Copyright 2010 The Royal Society of Chemistry. (i) Schematic of film formation by the spray pyrolysis technique. Reproduced from ref. 177. Copyright 2017 Springer Nature.

C/10 rate and good rate capability. Huang *et al.* presented electrospun $ZnCo_2O_4$ containing numerous nanopores (3 nm) as a high-performance lithium-ion battery anode material.[144] The resultant $ZnCo_2O_4$ nanotubes had a high reversible capacity of 1454 mA h g^{-1} at 100 mA g^{-1} and reached 794 mA h g^{-1} at a current density of 2000 mA g^{-1} after 30 discharge/charge cycles. In addition, Binan Lu and colleagues developed new 3D nanoporous $ZnWO_4$ nanoparticles using electrospinning for supercapacitors.[151] The electrode fabricated with 3D nanoporous $ZnWO_4$ nanoparticles could withstand a high current charge and discharge with a little capacitance fading, showing that the specific capacitance decreased by only 10% when the current density was increased from 40 A g^{-1} to 100 A g^{-1}.

The hard-template method, also known as nanocasting, is widely applied in the production of nanoporous oxide materials. The precursor molecules are injected into stiff molds to create the final nanoporous oxide product. As observed in Fig. 5a,[153] the rigid and porous template structure is impregnated with a mixture of metal precursors and chelating agents, which is then calcined and etched to remove the templates and produce the desired nanoporous oxide materials using acid or alkaline aqueous solution. Some specifications for templates are required to successfully synthesize desired products using nanocasting because the characteristics and quality of the templates and their interaction with the precursor determine the structure and morphology of the products. The templates should have stable, highly ordered porous structures and can be easily etched without affecting the properties of the product, so mesoporous silica (*e.g.*, SBA-15,[154–156] KIT-6,[154,157,158] MSU-H,[154] KCC-1,[159] and MCM-41 (ref. 159)) or mesoporous carbon (*e.g.*, CMK-1, and CMK-3) is commonly used as the porous hard template. Hard templating can be used on a variety of materials with high crystallinity due to the endurance of the stiff template to high temperatures and the ability to produce ordered and stable nanoporosity structures. However, the drawbacks of the hard template method include a reduced ability to adjust the pore size, resulting in a lower yield. Besides, the longer time necessary to

thoroughly introduce metal precursors into the template and the difficulty in completely removing the hard template using acid or alkaline solution are still disadvantages. Despite these issues, there have been a few publications on the fabrication of nanoporous oxide materials employing hard templating. For instance, using mesoporous silica KIT-6 as a hard template, 3D highly ordered nanoporous CuO was produced for high-performance asymmetric supercapacitors, as shown in Fig. 5b.[157] The highly ordered nanostructures are formed only when silica KIT-6 templates are present, according to the comparison of the TEM images of 3D highly ordered nanoporous CuO and bulk CuO shown in Fig. 5c–e. The electrode made from nanoporous CuO demonstrated outstanding electrochemical performance with a specific capacitance of 431 F g^{-1} at 3.5 mA cm^{-2}, retaining over 70% of capacitance when operated at 70 mA cm^{-2}. Im *et al.* reported the nanoporous TiO_2 preparation with several mesoporous silica templates (SBA-15, KIT-6, and MSU-H) for improved photovoltaic characteristics of DSSCs.[154] In comparison to nanocrystalline TiO_2, the nanoporous TiO_2 electrodes had a large surface area, a dye-adsorption capability that was 1.5 times higher, and greater photocurrent, fill factor, and solar energy conversion efficiency. Saeid Kadkhodazade and co-workers synthesized 3D-ordered nanocrystalline nanoporous $NiMoO_4$ by nanocasting it from mesoporous silica KIT-6 for high-performance supercapacitor electrode materials.[158] The nanoporous $NiMoO_4$-based electrode showed a high area-specific capacitance of 4.25 F cm^{-2} at 3 mA cm^{-2}, excellent rate capability of 2.18 F cm^{-2} at 120 mA cm^{-2}, excellent cycling stability in 6000 continuous cycles at different current densities exhibiting only 8.4% loss after 3000 cycles at 7.5 mA cm^{-2}, and high energy and power densities of 141.75 W h kg^{-1} at 0.6 kW kg^{-1} and 72.6 W h kg^{-1} at 24 kW kg^{-1}.

The use of soft templates has been widely described in the fabrication of nanoporous oxide materials, with the goal of co-assembly of surfactant molecules and inorganic species into ordered structures formed after removing the template, as illustrated in Fig. 5a.[153] Surfactants for soft-templating are amphiphilic compounds that reduce surface and interfacial tension and have hydrophobic and hydrophilic equivalents. There are three types of surfactants used for soft templates: cationic surfactant (*e.g.*, hexadecyltrimethylammonium bromide,[160] cetylpyridinium chloride, *etc.*), anionic surfactant (*e.g.*, sodium dodecyl sulfate, sodium dodecylbenzene sulphonate, *etc.*), and non-ionic surfactant (block co-polymer like PS-*b*-PEO,[161] Pluronic PE10300,[162] P-123,[163–165] polyvinylpyrrolidone (PVP),[166] *etc.*). Soft matter, composed of surfactants, organic molecules, and block copolymers, interacts with the precursors *via* weak non-covalent bonding such as van der Waals forces or hydrogen bonding. Three general methodologies for the production of soft-template nanostructures have been reported: cooperative self-assembly, liquid crystal templating, and evaporation-induced self-assembly.[153] The soft template method allows for the control of the morphology, size, and geometric structure, which is challenging with hard-template methods. Nonetheless, the fundamental obstacles in soft-templating are the limitation of crystal growth *via* heat treatment and the soft templates' low thermal stability. In addition, the complicated sol–gel processes and metal cation polymerization make detailed control of the porosity structure difficult. Fig. 5f shows the production process of the block copolymer PS-*b*-PEO templated nanoporous TiO_2 for quantum-dot-sensitized solar cells as a soft template, and Fig. 5g and h show the corresponding SEM images of nanostructured TiO_2 films on FTO glass.[161] The solar cell could attain a higher IPCE value and greater photovoltaic performance by optimizing the soft template to titanium precursor ratio, with a peak IPCE value of 21% and a power conversion efficiency of 0.358% under AM 1.5G. Dai *et al.* prepared nanoporous Mn_2O_3 using Pluronic P123 as a template for increasing the high-rate zinc storage performance in Zn-ion batteries.[164] The nanoporous Mn_2O_3 electrode exhibited a high reversible capacity of 233 mA h g^{-1} at 0.3 A g^{-1}, a superior rate capability of 162 mA h g^{-1} at 3.08 A g^{-1}, and exceptional cycling durability over 3000 cycles at a high current rate of 3.08 A g^{-1}. Li *et al.* presented nanoporous SnO_2 nanosheets as anode materials with PVP as a soft template for high-performance lithium-ion batteries.[166] The nanoporous SnO_2 nanosheets had an extremely high initial specific capacity of 2231 mA h g^{-1}, a specific capacity of 688 mA h g^{-1} after 60 cycles at a current density of 0.2 A g^{-1}, and an outstanding capacity retention of 224 mA h g^{-1} at 8 A g^{-1}.

The colloidal-template strategy, which involves incorporating inorganic species into organic polymer (*e.g.*, polystyrene (PS)[167] and poly(methyl methacrylate) (PMMA)[168,169]) templates, is an effective and alternative way of synthesizing oxide materials with ordered nanopores (Fig. 5a[153]). The colloidal template methods have several advantages over the soft-template methods, including the ability to produce highly ordered nanoporous oxides and the ability to calcine at a relatively high temperature. Colloidal-templating offers the synergetic characteristics of both hard and soft templates since the inorganic components serve as a hard template to confine desired materials and increase stability, and the polymer template acts as a soft template to organize the inorganic particles through self-assembly. Colloidal templating permits the formation of ordered nanostructures with controlled porosity, good crystallinity, and structural integrity at a relatively high calcination temperature. For example, Ko *et al.* prepared high-efficiency perovskite solar cells based on vertically oriented nanoporous TiO_2 employing PS-PMMA as a template.[168] The best solar cells based on 1D nanoporous TiO_2 nanorods showed an efficiency of 15.5% with an open-circuit voltage of 1.02 V, a short circuit current density of 20.0 mA cm^{-2}, and a fill factor of 76.1%. Wang *et al.* reported a nanoporous manganese oxide fabricated using a polystyrene template for use in supercapacitor applications.[169] The as-prepared nanoporous manganese oxide achieved a specific capacitance of 1018 F g^{-1} at a low current density of 500 mA g^{-1}, revealing the

prepared nanoporous manganese oxide as a viable candidate for supercapacitor applications. Even though colloidal templating has been extensively utilized for the synthesis of nanoporous oxide materials, several drawbacks limit its practical use. Because of the fragile properties of the material, the porous structure frequently collapses after the template removal, and the procedure is laborious and costly.

Spray pyrolysis is another adaptable synthesis process that is commonly used to produce nanoporous oxides (*e.g.*, aluminum oxide,[170] iron oxide,[171–173] tin oxide,[174,175] titanium oxide,[176] ruthenium oxide,[177] vanadium oxide,[178] copper-bismuth oxide,[179] cerium oxide[180]) based on thermal degradation of a liquid sample. In typical spray pyrolysis shown in Fig. 5i, the precursor solution is atomized into

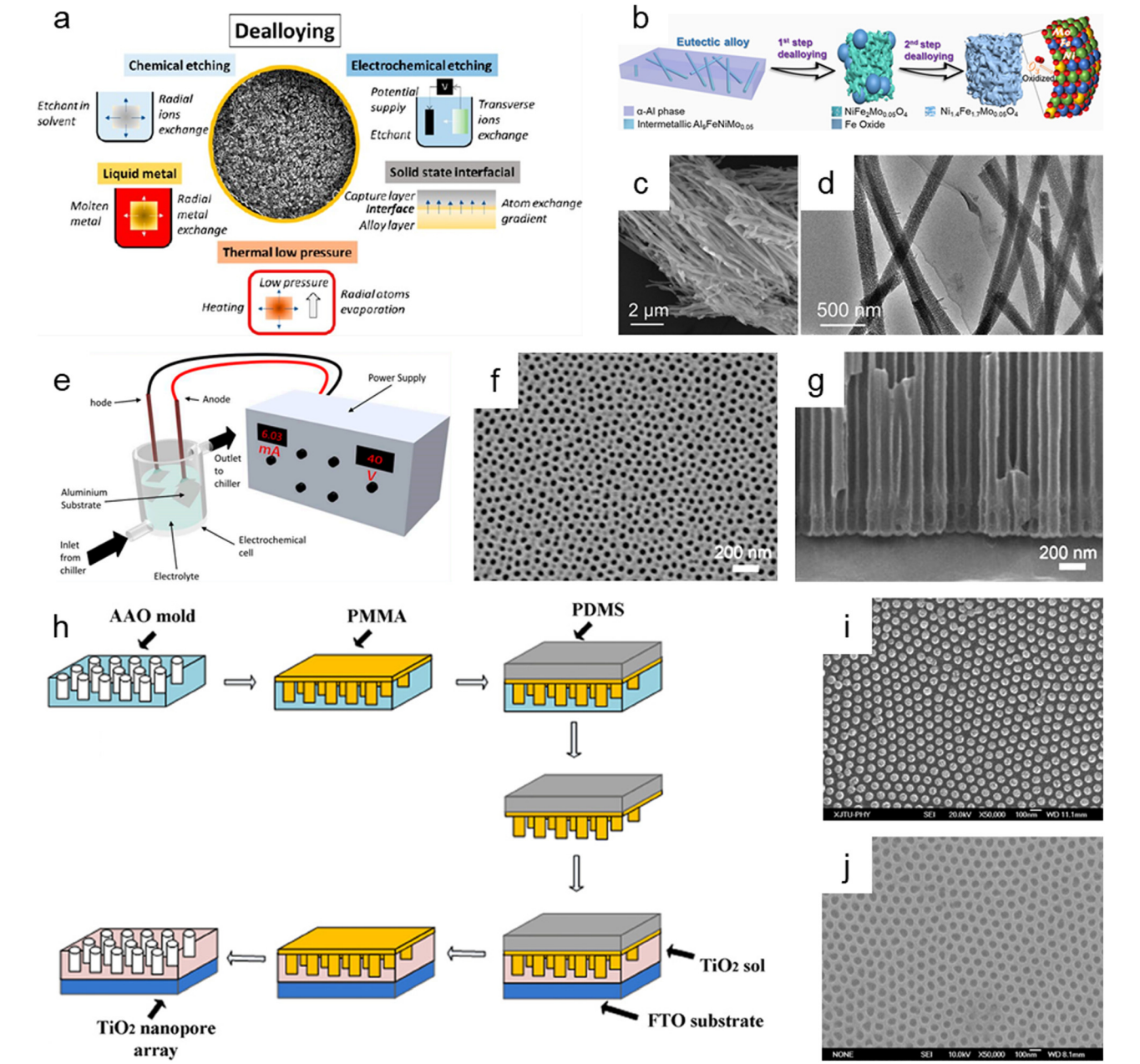

Fig. 6 Top-down synthesis methods of nanoporous oxides. (a) Summary of the main dealloying pathways. Reproduced from ref. 181. Copyright 2023 American Chemical Society. (b) Schematic illustration showing the dealloying process of the AlNiFeMo alloy in corrosive solutions to fabricate $Ni_{1.4}Fe_{1.7}Mo_{0.05}O_4$ nanowires. (c) SEM and (d) TEM images of $Ni_{1.4}Fe_{1.7}Mo_{0.05}O_4$ nanowires. (b–d) Reproduced from ref. 182. Copyright 2023 American Chemical Society. (e) Typical experimental setup for the fabrication of nanoporous anodic alumina (NAA). Reproduced from ref. 212. Copyright 2022 MDPI. (f) Plane view and (g) cross-sectional SEM micrographs of AAO. Reproduced from ref. 200. Copyright 2011 Elsevier. (h) Schematics of the fabrication process of the nanoimprinted TiO_2 nanopore arrays. (i) Top SEM image of the PMMA mold obtained from the AAO mold. (j) Top SEM image of the nanoimprinted TiO_2 nanopore arrays with a diameter of 50 nm and an interpore distance of 100 nm. (h–j) Reproduced from ref. 213. Copyright 2011 Elsevier.

small droplets and delivered to the heated substrates as a form of vapor, creating thin films on the substrates.[177] The spray pyrolysis approach allows for precise control of the properties of the product by adjusting the spray rate, air flow rate, solution concentration, droplet size, and distance from the nozzle to the substrate. Among these, the droplet size and deposition temperature have a major effect on the surface morphology and thickness of the film. Spray pyrolysis is an intriguing technology for producing nanoporous oxide materials since it allows for great thin-film adhesion on large substrates and homogeneity. Fig. 5i provides a schematic representation of the formation of thin films using the spray pyrolysis process together with both the schematic and actual surface micrographs of the thin films.[177] The spray pyrolysis process was employed to load the nanoporous ruthenium oxide electrode on thin stainless steel substrates, which were then used as free-standing electrodes for supercharged capacitors. The electrodes made of nanoporous ruthenium oxide had an ultrahigh specific capacitance of 1429 F g^{-1} at a scan rate of 1 mV s^{-1}, a higher energy density of 172 W h kg^{-1}, a power density of 320 kW kg^{-1}, a columbic efficiency of 94.74% in 1 M KOH, and a low charge transfer resistance of 0.89 Ω. U. J. Chavan and co-workers reported hematite α-Fe_2O_3 thin films made by a spray pyrolysis approach for the electrochemical supercapacitive performance.[171] The α-Fe_2O_3 thin film electrodes had a maximum specific capacitance of 451 F g^{-1} within the potential window of −1.1 to 0.2 V in an aqueous 2 M KOH electrolyte and a 1.3 V voltage window with a specific energy and a specific power of 45 W h kg^{-1} and 1.25 kW kg^{-1} at 4 A g^{-1}, respectively. R. M. Gamini Rajapakse *et al.* prepared fluoride-doped tin oxide on soda-lime glass films by using a specially designed atomized spray pyrolysis process for the operation of DSSCs.[175] The synthesized FTO films provided an electronic conductivity of 1.17×10^3 S cm^{-1}, an electron mobility of 10.89 cm^2 V^{-1} s^{-1}, a carrier density of 9.797×10^{20} cm^{-3}, and a maximum light-to-electricity efficiency of 10.4% under AM 1.5 illumination for a cell active area of 0.25 cm^2.

3.2. Top-down methods

Dealloying is a cutting-edge method that relies on the selective removal of sacrificial metal components from an alloy structure to produce nanoporous oxide materials under particular environmental conditions. As presented in Fig. 6a, dealloying can be achieved through chemical etching,[3,181–186] electrochemical processing,[181,187–190] immersion in liquid metal,[181,191–193] and solid-state stripping,[181,194–196] as well as by vapor-thermal processing.[181,197–199] The metal atoms in the primary alloy are changed into metallic ions by localized oxidation when nanoporous oxide materials are produced using dealloying procedures. These metallic ions are then released in the dealloyed result. The morphology and surface properties of the dealloyed result can be determined by the atomic rearrangement and reaction kinetics, which are governed by input energy to deconstruct the metal alloy, reaction environment, and starting alloy composition. In particular, adjusting the conditions under which a sacrificial metal is removed, as well as the characteristics of the bulk alloy, can change the size distribution, volume, and interconnectivity of pores.

Chemical dealloying is a procedure that involves a liquid-based redox reaction with the help of either an electrical supply or an acid or a base. On the other hand, electrochemical dealloying relies on selective etching using an electric field at a neutral pH environment. The primary distinction between the two etching methods is the kind of initial chemically dealloyed species, which is the atoms with fewer noble metal atoms in chemical dealloying *versus* atoms with lower corrosion potential in electrochemical dealloying. In liquid metal dealloying, the sacrificial metal is removed from the solid metal alloy while the alloy metals are still solid at high temperatures. Solid-state interfacial dealloying is accomplished by making contact between the dealloying agent and the alloy at a low temperature to promote interfacial diffusion and remove the sacrificial metal *via* solid-state transfer. Vapor-thermal dealloying is a process that requires selectively evaporating one of the sacred metal phases in a vacuum, resulting in the formation of vacancy sites. These vacancies offer routes for regional rearrangements and migrations of the noblest metal atoms still present in the system, which lowers the surface energy. Fig. 6b shows the preparation of nanoporous $Ni_{1.4}Fe_{1.7}Mo_{0.05}O_4$ nanowires *via* a two-step chemical dealloying procedure in which the AlNiFeMo alloy was immersed in corrosive solutions.[182] Fig. 6c and d illustrate the SEM and TEM images of the nanoporous $Ni_{1.4}Fe_{1.7}Mo_{0.05}O_4$ nanowires, which have an average diameter of 200 nm and a length of over 10 μm with an average pore/ligament size of around 4 nm. The 3D Mo-doped nanoporous NiFe oxide nanowires exhibited an efficient electrocatalytic oxygen evolution reaction performance with a low overpotential of 205 mV at 10 mV cm^{-2} and a small Tafel slope of 51.3 mV dec^{-1}.

Anodization has emerged as one of the most popular synthesis techniques of various nanoporous oxides (*e.g.*, aluminum oxide,[200,201] titanium dioxide,[202–204] tin oxide,[205,206] tungsten oxide,[207] tantalum pentoxide,[208] vanadium pentoxide,[209,210] and niobium oxide[211]) with well-controlled pores due to its distinctive electrochemical properties, large surface area, and high thermal stability. A typical electrochemical setup is required for anodizing the surface of a metal, which includes a chiller to maintain low-temperature conditions for the electrolyte, cathode metals, and high-purity metal foil for the anode, as well as an external power supply for galvanostatic or potentiostatic anodization, as shown in Fig. 6e.[212] By adjusting the reaction parameters including the type, content, and concentration of electrolytes, applied potential/current, and temperature, the metal's surface is transformed in this electrolytic oxidation process into an oxide or hydroxide with the desired porosity. The porosity of the resulting oxide depends on the type of electrolyte used, and acidic electrolytes can produce

nanoporous oxides. For example, C. T. Lee *et al.* used one-step anodization to create nanoporous anodic aluminum oxide films to evaluate the impacts of temperature and voltage mode on anodization processes.[200] Al foil was anodized in one step using hybrid pulse anodization (HPA) and direct current anodization in 0.5 M oxalic acid at a temperature of 5–15 °C. As shown in Fig. 6f and g, which depict the SEM micrographs of the top-view and cross-section of the anodic aluminum oxide (AAO) formed by one-step HPA from 99.997% Al foil for 1 h at a temperature of 15 °C, a well-formed semicircle structure without cracks or voids at the interface between AAO and Al foil is achieved with pore diameters in the range of 45 ± 5 nm. For a supercapacitor electrode material, Han *et al.* described self-organized nanoporous tin oxide films made by anodizing a tin substrate in an aqueous electrolyte containing oxalic or phosphoric acid.[206] The fabricated nanoporous tin oxide films had a maximum specific capacitance of 274 F g^{-1} and a long life in electrochemical charge/discharge cycles. Furthermore, Li *et al.* prepared oxygen-deficient Ta_2O_5 nanoporous films as self-supported electrodes for lithium microbatteries by electrochemical anodization of tantalum metal in an ammonium fluoride electrolyte and subsequent thermal annealing.[208] The prepared nanoporous Ta_2O_5 films showed a high lithium capacity of about 480 mA h g^{-1} and exceptional cycling stability over 8000 cycles at a rate of 5C.

Imprinting, in which the structure and morphology of the material are pre-determined by the template containing nanopores, is another helpful method for synthesizing nanoporous oxide materials. By using the imprinting method, the nanostructure can be replicated by mechanical contact and 3D material displacement.[213] In a typical imprinting procedure, a thin coating of polymer materials is applied to the template's surface to penetrate its pores and produce a stable structure that will help with the subsequent steps of mold construction. The flexible and highly elastic polymer materials are then injected onto the surface of the as-prepared sample to create a mold and replicate the desired patterns or structures in the following imprinting operations. After removing the template, the constructed mold is used to apply the necessary components to the sol while maintaining a constant applied pressure and temperature. The mold is subsequently removed, and nanoporous oxide structures are then calcined at a high temperature. X. Hu *et al.* reported a nanoimprinted TiO_2 nanopore array for photovoltaic applications as an example of a nanoporous oxide material synthesized using an imprinting process.[213] Fig. 6h shows the typical fabrication process of the nanoporous TiO_2 array, directly nanoimprinted on an FTO glass substrate using a PMMA/PDMS composite soft template, which is replicated from an AAO replica mold. Fig. 6i shows the top SEM images of the PMMA mold made from the AAO mold, demonstrating that the PMMA mold was highly ordered, and the sizes were accurately matched to the equivalent AAO molds. As shown in Fig. 6j, the replication from the PMMA/PDMS mold to the nanoporous TiO_2 arrays was successful since the pore diameters of the nanoimprinted TiO_2 nanopore arrays matched those of the respective AAO templates. The solar cells combined with the TiO_2 nanopore arrays demonstrated that they might be more effective in quenching photoluminescence emission with a maximum efficiency of about 0.32% for a photovoltaic device. Kim *et al.* described highly ordered nanoimprinted TiO_2 with nanopores for hybrid inverted bulk heterojunction solar cells.[214] The as-synthesized solar cells showed a higher power conversion efficiency of 1.49% than on a flat titania of 1.18%.

All of the synthesis methods for nanoporous oxide materials discussed above have benefits, drawbacks, and limitations. Various synthetic strategies have been employed in previous studies to produce nanoporous oxides and examine their properties; however, utilizing these approaches completely to precisely regulate the structure and properties of nanoporous oxides remains a challenging task. Novel and simple strategies for thoroughly regulating nanoporous structures while ensuring structural uniformity and stability need yet to be developed for further practical applications of nanoporous oxide materials. For example, by properly integrating these distinct fabrication techniques, novel perspectives into the synthesis and control of intrinsic oxide nanoporous materials can be accomplished. Electrospinning can be used to produce nanoscale fibers, which can subsequently be applied to a dealloying process to generate a variety of metal-oxide nanoporous structures. These structures are intended to offer innovative solutions in a variety of applications through enhancing surface area, structural stability, and electrical properties. Current research on nanoporous oxide synthesis methods is expected to result in revolutionary advances in future nanotechnology and nanomaterial applications, as well as provide a new research direction in the field of nanoporous oxide synthesis and contribute to the development of innovative nanoporous oxide materials.

4. Applications of nanoporous oxide electrodes

4.1. Energy conversion devices

4.1.1. Fuel cells. A fuel cell is a representative energy conversion device that generates electricity through the electrochemical reaction between the fuel and oxidant without combustion. Among various fuel cells, the solid oxide fuel cell (SOFC) using a solid ceramic electrolyte is a device in which nanoporous oxides play several crucial roles. The triple phase boundary (TPB) is the region in SOFCs where three phases intersect: electrolytes, electrodes, and reactant gases.[215] Since the TPB provides an active zone where several processes, such as ion transport, gas diffusion, and catalytic reactions, occur simultaneously, it has a crucial role in facilitating the electrochemical reactions that occur within the SOFC.[216] The efficiency and performance of the SOFC greatly depend on the characteristics of the TPB. Factors such as its length, density, and accessibility influence the rate of

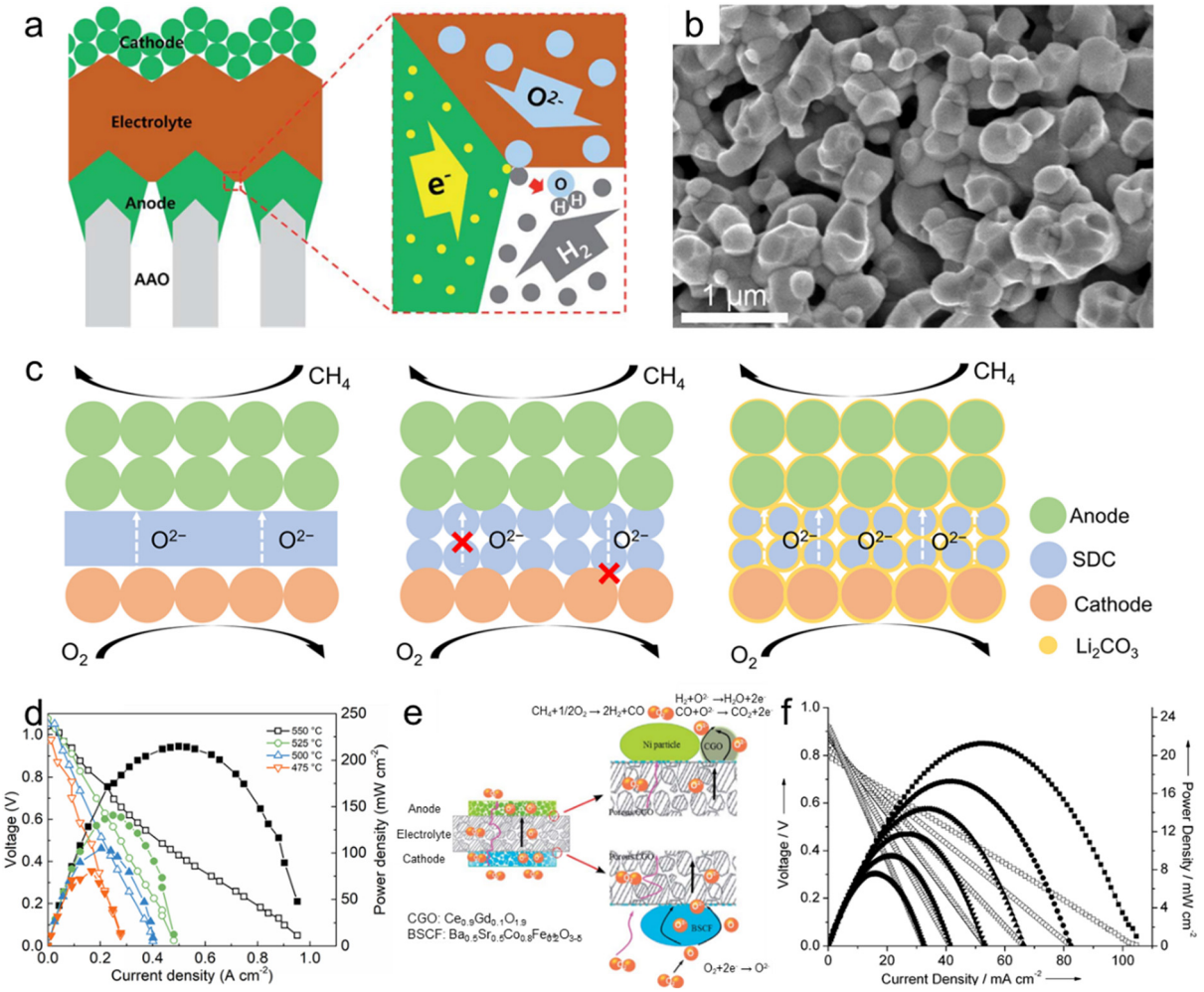

Fig. 7 Nanoporous oxide electrodes for fuel cells. (a) Schematic showing the structure of a thin-film-based solid oxide fuel cell supported on an anodic aluminum oxide (AAO) template and the transport of gases, oxygen ions and electrons near the electrodes and the electrolyte. Reproduced from ref. 218. Copyright 2017 The Royal Society of Chemistry. (b) Cross-sectional SEM image of the LSTN-YSZ contact layer. Reproduced from ref. 219. Copyright 2023 Springer Nature. (c) Schematic of the SOFC, porous SOFC, and the CSSFC. (d) *I–V* and *I–P* curves of the CSSFC in CH_4 at different temperatures. Reproduced from ref. 225. Copyright 2022 PNAS. (e) Schematic representation of the all-porous $Gd_{0.1}Ce_{0.9}O_{1.9}$ (CGO)-supported fuel cell. (f) *I–V* and *I–P* curves of the all-porous fuel cell under a 4% CH_4–96% He/4% O_2–96% N_2 atmosphere at different temperatures. Reproduced from ref. 226. Copyright 2013 The Royal Society of Chemistry.

electrochemical reactions and overall cell performance.[217] Nanoporous oxides maximize the TPB length and ensure its accessibility to reactant gases.[7] The nanoporous oxides can serve as a support material for catalysts in SOFC electrodes. The high surface area not only facilitates the dispersion of catalytic particles but also allows the reactant gases to reach the TPB. Ji *et al.* designed a Ni-based electrode on a porous alumina template.[218] As shown in Fig. 7a, the introduction of AAO increased the length of the TPB where electrons, fuel, and the oxidant were in contact, and the microstructure, electrical conductivity, and H_2 permeability changed depending on the deposition conditions of Ni. Kwon *et al.* also fabricated micro-SOFCs by depositing Pt electrodes on nanoporous AAO templates.[2] The microstructures contributed to the open circuit voltage (OCV) of 1.02 V and the maximum power density (MPD) of 350 mW cm^{-2} at 500 °C. Kim *et al.* designed a new dual-layer oxide-based substrate of (La,Sr)(Ti,Ni)O_3-yttria-stabilized zirconia (LSTN-YSZ) by simple co-firing. As shown in the SEM image (Fig. 7b), the LSTN-YSZ with small and uniform pore sizes under 500 nm was uniformly formed on the porous stainless steel substrate.[219] The YSZ-based SOFC recorded a high power density of 560 mW cm^{-2} at 550 °C for 13 hours.

The second role of nanoporous oxides is as an electrolyte matrix. Various nanoporous oxides, such as yttria-stabilized zirconia (YSZ),[220] gadolinium-doped ceria (GDC),[221] scandia-stabilized zirconia (SSZ),[222] and samarium-doped ceria (SDC),[223] are commonly used as the electrolyte material in SOFCs. The nanoporous structure of these oxides provides a high surface area and interconnected pathways for oxygen ion transport. This enables efficient ion conduction through the electrolyte, facilitating the electrochemical reaction within the SOFC. Liu *et al.* developed a heterostructure electrolyte based on $Gd_{0.15}Ni_{0.05}Ce_{0.8}O_{2-\delta}$ (GNDC) and

SnO_2.[224] The GNDC–SnO_2 composite consisted of nanoscale particles, which offered sufficient grain boundaries and surface area. Based on the high ionic conductivity of 0.124–0.220 S cm^{-1}, the fuel cell with the GNDC–SnO_2 electrolyte recorded an OCV of 1.026 V and a high MPD of 879.4 mW cm^{-2} at 550 °C. Su *et al.* proposed a carbonate-superstructured solid fuel cell (CSSFC) with a tuned electrolyte as an advancement of the conventional SOFC.[225] The *in situ* generation of the superstructured carbonate (Li_2CO_3) during the operation in SDC showed a high ionic conductivity of 0.17 S cm^{-1} at 550 °C. Fig. 7c illustrates the mechanism of the CSSFC. In nanoporous electrolytes of the SOFC, the specific area is larger than that of dense electrolytes, but it can lead to increased contact resistance between electrodes and require higher operating temperatures. On the other hand, incorporating molten carbonate into the nanoporous electrolyte improves oxygen ion conduction by creating a continuous interface between molten carbonate and solid ionic conductors. Additionally, it would establish a robust connection near the electrode–electrolyte interface. As shown in Fig. 7d, the CSSFC with the porous SDC electrolyte achieved a high OCV of 1.041 V and MPD of 215 mW cm^{-2} at 550 °C in dry methane fuel. Based on porous electrolytes and electrodes, Guo *et al.* suggested an all-porous SOFC.[226] As shown in Fig. 7e, a porous $Ce_{0.9}Gd_{0.1}O_{1.9}$ (CGO) electrolyte prepared by dry pressing was combined with a porous $Ba_{0.5}Sr_{0.5}Co_{0.8}Fe_{0.2}O_{3-\delta}$ (BSCF) cathode and a Ni particle anode. Oxygen flows from the cathode and is diffused by the porous electrolyte to the catalytic anode while methane is fed at the anode. The porous CGO electrolyte microstructure enhanced the ionic conductivity and increased the power density of the SOFC. As shown in Fig. 7f, the all-porous SOFC with the porous CGO electrolyte recorded an OCV of 0.8 V and MPD of 21.4 mW cm^{-2} at 750 °C. We summarized the materials, OCV, MPD, and operating temperatures of fuel cells in Table 1. Nanoporous oxide electrodes have significantly enhanced the electrochemical performance of SOFCs. Their high surface area and tailored pore structures could enable more efficient fuel oxidation and oxygen reduction reactions, resulting in higher power output and improved cell efficiency. Future research might focus on developing nanoporous oxide electrodes that enable SOFCs to operate at reduced temperatures. This advancement would lead to shorter start-up times, longer lifespan, and improved thermal management, making SOFCs more practical for a wider range of applications.

4.1.2. Water splitting electrodes. Water splitting, which decomposes water into hydrogen and oxygen, is a promising technology as the reverse reaction of fuel cells since it converts the applied energy into clean and sustainable chemical energy, hydrogen.[227,228] Among the reactions involving electrodes, it is classified into two categories: electrochemical (EC) water splitting and photoelectrochemical (PEC) water splitting, depending on the input energy.[229] Both systems, based on surface catalytic reactions, share a common principle where introducing nanoporous oxide electrodes increases the specific surface area, thereby enhancing the characteristics by increasing the active sites.[230,231] However, in the case of PEC water splitting, where additional photovoltage is involved based on sunlight, the importance of nanoporous oxides is even greater in terms of light absorption and charge separation aspects. When light irradiates, scattering on the surface of nanoporous oxides increases the absorbance of the photoelectrodes.[232] Furthermore, the diffusion path of photogenerated minority

Table 1 Electrochemical performance of nanoporous oxide electrodes in energy conversion devices

Fuel cells

Materials	OCV [V]	MPD [mW cm^{-2}]	Temperature [°C]	Ref.
Ni-YSZ (AAO template)	1.0	28	500	218
Pt-YSZ (AAO template)	1.02	350	500	2
LSTN-YSZ (STS template)	1.05	560	550	219
NiO-YSZ	1.04	187	600	220
NiO-GDC	1.0	178	800	221
Ni-SSZ	1.1	150	600	222
NiO-BZCYYb	1.047	640	650	223
SnO_2-GNDC	1.026	879.4	550	224
Ni-BZCYYb-SDC	1.041	215	550	225
NiO-CGO	0.8	21.4	750	226

Solar cells

Materials	V_{oc} [V]	J_{sc} [mA cm^{-2}]	PCE [mW cm^{-2}]	Ref.
Ag–TiO_2 NTA	0.882	6.41	4.02	253
TiO_2 MS	0.712	17.69	9.29	254
TiO_2 SPs	0.808	17.98	10.66	256
h-TiO_2/LPP	0.824	14.69	8.05	257
SnO_2 NP/ZnO HS	0.632	11.01	4.37	261
TiO_2/ZnO NRs	0.63	6.73	2.68	262
rGO/NiO	0.125	2.6	0.11	265

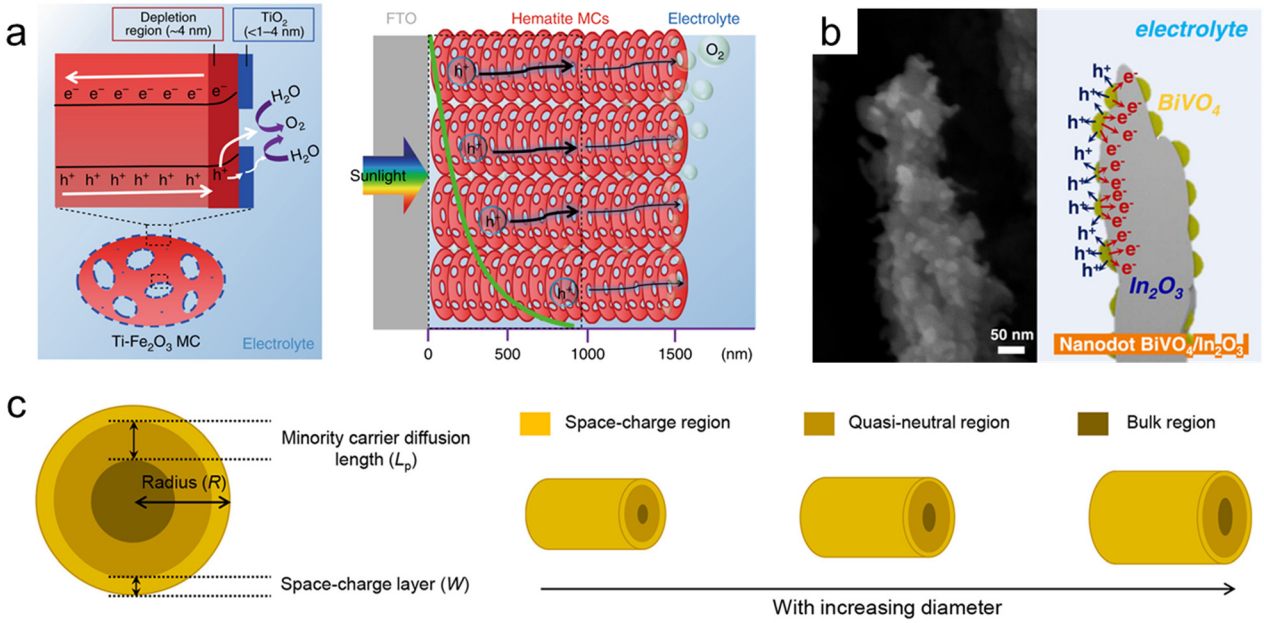

Fig. 8 Nanoporous oxide electrodes for water splitting. (a) Illustration of charge carrier dynamics in a thick hematite mesocrystal (MC) film. Reproduced from ref. 236. Copyright 2019 Springer Nature. (b) Cross-sectional SEM image and illustration of nanodot $BiVO_4/In_2O_3$ nanorods. Reproduced from ref. 247. Copyright 2023 Wiley. (c) Relationship between the minority carrier diffusion length (L_p) and the particle diameter. Reproduced from ref. 248. Copyright 2021 American Chemical Society.

carriers to the surface is reduced to below their diffusion length, resulting in improved charge transport.[233]

Hematite (α-Fe_2O_3), one of the most representative photoanode materials, has a low band gap of 2.1 eV, resulting in high theoretical photocurrent density. However, its actual efficiency is low due to a very short hole diffusion length of a few nanometers. Therefore, nanostructuring is essential in utilizing hematite-based photoanodes.[234,235] Zhang *et al.* fabricated thick hematite films (~1500 nm) constructed from highly ordered hematite mesocrystals (MCs) with solvothermal methods.[236] As shown in Fig. 8a, the excellent penetration of the electrolyte into the mesoporous film and the increased specific surface area resulted in a larger depletion region compared to the Fe_2O_3 single crystal. The thin TiO_2 layer formed on the surface of the MCs induced a steeper band banding, maximizing charge separation. Yoon *et al.* synthesized a Ge-doped porous Fe_2O_3 photoanode by immersing β-FeOOH based on the solution process in a Ge solvent followed by heat treatment.[237] It exhibited higher porosity compared to Ge-doped hematite formed through a one-step process, and after coating a $NiFeO_x$ catalyst, it showed a high photocurrent density of 4.6 mA cm^{-2} at 1.23 V_{RHE}. Jang *et al.* controlled the thickness and porosity of Fe_2O_3 through multiple regrowth processes using heat treatment of the synthesized FeOOH.[234] It was first combined with a Si photocathode, and the tandem device achieved a solar-to-hydrogen (STH) conversion efficiency of 0.91%. By doping Ta into hematite nanorods through hydrothermal regrowth and hybrid microwave annealing, Zhang *et al.* obtained a high photocurrent density of 3.22 mA cm^{-2} at 1.23 V_{RHE}.[238]

Bismuth vanadate ($BiVO_4$) is a promising photoanode material with a band gap of 2.4 eV. However, its short hole diffusion length of 70 nm leads to degradation of the PEC performances due to charge recombination. To overcome this challenge, most studies have introduced nanoporous $BiVO_4$.[239,240] McDonald *et al.* synthesized nanoporous $BiVO_4$ for the first time using electrodeposited BiOI.[241] When the 2-dimensional plate-lick BiOI crystals were annealed together with a V-based precursor, they formed a few hundred-nanometer nanopores in $BiVO_4$. Furthermore, Lee *et al.* obtained denser BiOI nanoplates by separating the electrodeposition process into nucleation and growth steps. Additionally, lactate buffer induced a uniform increase in local pH, resulting in a more uniform film formation and smaller nanopores in $BiVO_4$.[242] To further maximize the specific surface area of the existing nanoporous $BiVO_4$, Yang *et al.* first introduced SnO_2 nanorods underneath the $BiVO_4$ layer.[243] $BiVO_4$ was vertically formed along the nanorods, and due to the coexistence of mesopores formed by SnO_2 and nanopores of $BiVO_4$, the $BiVO_4/SnO_2$ photoanode achieved a high photocurrent density of 6.3 mA cm^{-2} at 1.23 V_{RHE}. Lee *et al.* synthesized various nanostructures of $BiVO_4$ without BiOI precursors using a one-step synthesis method called pulsed electrodeposition.[244–246] Also, In_2O_3 nanorods were first introduced as an electron transport layer for $BiVO_4$ through glancing angle deposition.[247] By adjusting the pulse cycle of electrodeposition, the coverage of $BiVO_4$ was controlled, and a transition from a nanodot to a core–shell structure was observed at the specific cycle. As shown in the cross-sectional SEM image (Fig. 8b), $BiVO_4$ nanodots have a larger specific surface area compared to the core–shell

structure, increasing contact with the electrolyte. Also, nanodots below the diffusion length of $BiVO_4$ resulted in the suppression of charge recombination and led to a high charge collection ability. Bera *et al.* conducted a more detailed analysis of the relationship between the minority carrier diffusion length (L_p) and particle diameter.[248] As shown in Fig. 8c, as the radius of $BiVO_4$ increases, the bulk region also increases, deteriorating the PEC performances since the probability of holes escaping bulk recombination in oxides is proportional to e^{x-}/L_p. When the particle radius (R), except for the space charge layer (W) influenced by the drift, is smaller than the diffusion length, the bulk recombination is suppressed, causing high charge separation efficiency. Nanoporous oxide electrodes have enhanced light absorption in water splitting photoelectrodes. Their high surface area and tailored porosity allow for efficient light trapping and increased charge separation, improving solar-to-hydrogen conversion efficiency. Developing nanoporous oxide electrodes that exhibit enhanced stability under prolonged photoelectrochemical operation will be a key goal. These electrodes could resist degradation from factors like photocorrosion, ensuring longer-lasting and reliable water splitting performance.

4.1.3. Solar cells. Among various solar cells that convert sunlight into electricity, DSSCs are a prominent example of oxide-based devices. DSSCs, consisting of a semiconductor electrode, sensitizer, redox electrolyte, and counter electrode, generate electric current as the photogenerated charges, created when sunlight reaches the sensitizer molecules and oxide semiconductor, are separated and transported.[249] The nanoporous oxides in DSSCs play several crucial roles in the overall functioning of the device.[250] The increased surface area maximizes light absorption, enhancing the overall efficiency of the solar cell. Also, the nanoporous oxides provide sites for the adsorption of light-absorbing sensitizers. These dyes are responsible for capturing photons from sunlight and initiating electron transfer within the solar cell. Furthermore, the interconnected network of nanopores within the oxide semiconductor allows for rapid and efficient transport of the separated electrons. The nanoporous structure also allows for the penetration of the redox electrolyte into the oxide semiconductor, facilitating the replenishment of the sensitizers' oxidized state with electrons from the electrolyte. This ensures the continuous operation of the DSSCs.

Since the sensitizer is designed to absorb photons in the visible light region, semiconductor electrodes generally use wide band gap materials capable of absorbing the ultraviolet region in order to achieve efficient light harvesting.[251] TiO_2, which possesses a wide band gap (3.2 eV), high electron mobility, and stability, is the most representative material, and various TiO_2 nanostructures based on solution processes have been developed for DSSCs.[252] Choudhury *et al.* formed TiO_2 nanowires through a hydrothermal reaction and synthesized hierarchical nanoforest structures of TiO_2 using a second acid-assisted hydrothermal reaction.[253] As shown in Fig. 9a, it is observed that TiO_2 nanoarrays are densely formed along the Ti wire, maximizing the contact area with the electrolyte. Ag nanoparticles were synthesized on the TiO_2 nanoforest by photon-assisted reduction, giving a 16.1% increase in efficiency compared to nanotree array (NTA)-based DSSCs. The device recorded a short circuit current density (J_{sc}) of 5.98 mA cm^{-2}, which originated from the enhanced absorbance by the TiO_2 nanostructures and the SPR effect of Ag nanoparticles. TiO_2 NPs have numerous grain boundaries but low surface area. On the other hand, TiO_2 nanospheres (SPs) have a high surface area but difficulty in charge transport at the SP interfaces. Therefore, the optimal size of SPs that combines the advantages of both structures is challenging.[254,255] Yu *et al.* discovered the optimal size of porous TiO_2 nanospheres (SPs) for achieving high power conversion efficiency (PCE) in DSSCs.[256] Porous TiO_2 SPs with sizes ranging from 100 to 200 nm were synthesized through the control of hydrolysis conditions during the sol–gel reaction. The DSSC consisting of SP100 with SP450 as a light scattering layer exhibited a high PCE of 10.66%. Kang *et al.* introduced hierarchical TiO_2 (h-TiO_2) with polyvinylpyrrolidone as a pore-forming agent to further enhance light absorption and the PCE of conventional mesoporous TiO_2 (m-TiO_2).[257] It has been revealed that h-TiO_2, which coexists with macropores, offers advantages over

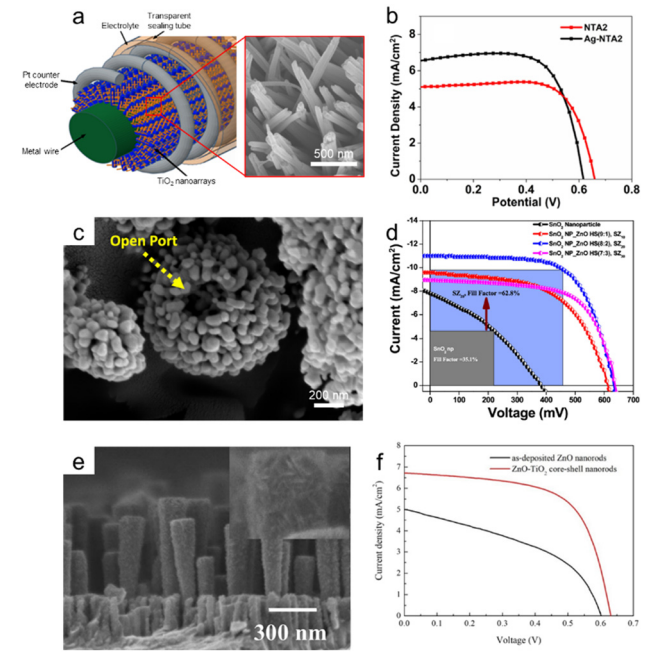

Fig. 9 Nanoporous oxide electrodes for solar cells. (a) Scheme of the TiO_2 nanoarray-based dye-sensitized solar cell (DSSC). (b) *J*–*V* curves of nano-tree TiO_2 and Ag deposited nano-tree TiO_2 DSSCs. Reproduced from ref. 253. Copyright 2021 Springer Nature. (c) FESEM image of ZnO hollow nanospheres. (d) *J*–*V* plots for DSSCs of SnO_2 nanoparticles with different ZnO hollow nanospheres. Reproduced from ref. 261. Copyright 2018 American Chemical Society. (e) FESEM image of ZnO–TiO_2 core–shell nanorods. (f) *J*–*V* characteristics of DSSCs applying ZnO nanorods and ZnO–TiO_2 core–shell nanorods. Reproduced from ref. 262. Copyright 2020 MDPI.

m-TiO_2 in terms of diffusion and electrolyte injection. The optimized DSSCs consisting of h-TiO_2 photoanodes with a long-persistence-phosphor layer showed the highest PCE of 8.05%.

SnO_2 and ZnO, which have wide band gaps, have also been extensively studied in DSSCs for UV absorption, although their electron injection rates are lower compared to that of TiO_2.[258–260] Banik *et al.* synthesized mesoporous hollow ZnO microspheres (HS) using the wet chemical process, as shown in Fig. 9c.[261] It was used as the photoanode in DSSCs by forming composites with SnO_2 NPs synthesized through a reflux process. ZnO HS exhibited excellent light scattering, and DSSCs recorded a high J_{sc} of 7.82 mA cm^{-2} by utilizing a synergistic effect at the optimal mixing ratio with SnO_2 NPs (Fig. 9d). Zhang *et al.* introduced a core–shell structure of TiO_2-coated ZnO nanorods deposited using sputtering.[262] As shown in the SEM image (Fig. 9e), the TiO_2 nanostructures deposited by mist chemical vapor deposition are observed to be formed around the ZnO nanorods, leading to increased roughness and surface area of the photoanode. NiO, which has a band gap of 3.6 eV, is generally used as a photocathode in DSSCs.[263,264] Zannotti *et al.* introduced rGO to enhance the performances of NiO NPs formed by the sol–gel process.[265] The rGO coated on the surface of NiO through the thermal reduction of GO not only increased the surface area and mesopore volume but also contributed to the improvement of electron transport. We summarized the materials, V_{oc}, J_{sc}, and PCE of DSSCs in Table 1. Nanoporous oxide electrodes have enhanced light-harvesting capabilities in DSSCs. Their large surface area and well-defined porosity provided ample sites for dye molecule absorption, allowing for increased photon capture and improved overall PCE. Future research might focus on tailoring the pore structures of nanoporous oxide electrodes to optimize dye loading and electron transport. By precisely controlling the pore size and distribution, researchers can fine-tune the interaction between the dye molecules and the electrode, leading to improved charge separation and collection. Also, as DSSCs move closer to large-scale implementation, the development of scalable fabrication methods for nanoporous oxide electrodes will become crucial. Innovations in electrode production could help meet the growing demand for cost-effective and efficient solar energy solutions.

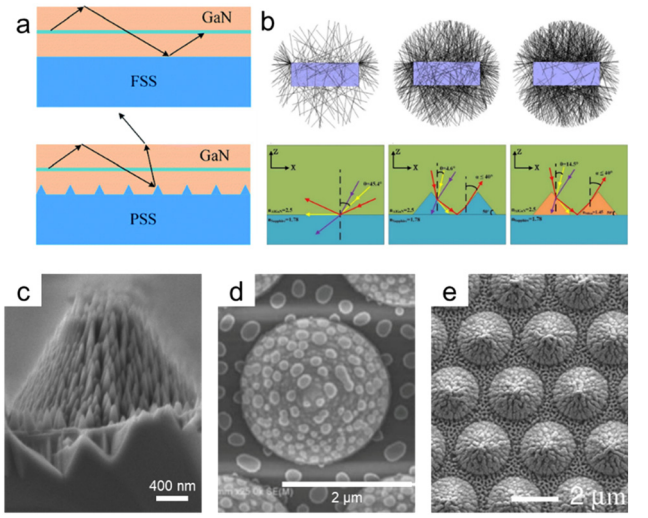

Fig. 10 Nanoporous oxide electrodes for light-emitting diodes. (a) Schematics of light trajectories in LEDs with the flat sapphire substrate (FSS) and patterned sapphire substrate (PSS). Reproduced from ref. 268. Copyright 2022 The Royal Society of Chemistry. (b) Cross-sectional ray-tracing images and schematic illustration of light trajectories of UV-LEDs on the FSS, PSS, and PSSA. Reproduced from ref. 269. Copyright 2020 Elsevier. (c) Cross-sectional SEM image of the nano–micro complex PSS (NMCPSS). Reproduced from ref. 273. Copyright 2016 American Chemical Society. (d) SEM image of the micro–nano PSS (MNPSS). Reproduced from ref. 274. Copyright 2013 IOP Science. (e) SEM image of the hybrid PSS. Reproduced from ref. 275. Copyright 2016 American Chemical Society.

4.1.4. Light-emitting diodes. Nanoporous oxides can play a significant role in LEDs that convert electric current into light in various ways. First of all, nanoporous oxides contribute to light extraction enhancement. The high surface area and porosity help to scatter and redirect light that would otherwise be trapped within the LED structure.[10] By increasing the extraction efficiency, nanoporous oxides improve the overall brightness and luminous efficiency of the LED device. The representative material used as the light extraction layer is a patterned sapphire substrate (PSS).[266] The light escape cone refers to the angular range within which light emitted from the LED can escape the device and be effectively emitted into the surroundings.[267] It is determined by the refractive index of the LED materials and the critical angle at which total internal reflection occurs. In a flat sapphire substrate (FSS), if the light reaches an interface at an angle greater than the critical angle, it will be totally internally reflected and unable to escape the LED, as shown in Fig. 10a.[268] However, the PSS helps redirect the internally reflected light toward angles within or beyond the escape cone, allowing a larger fraction of the light to be emitted from the LED. Hu *et al.* compared the light-escaping ability of various substrates.[269] InGaN/AlGaN-based LEDs were fabricated on a FSS, PSS, and patterned sapphire substrate with silica arrays (PSSA). As shown in Fig. 10b, the LED on the PSSA showed enhanced emission to vertical directions and reduced emission from the side facets compared to those on the FSS and PSS. According to the light trajectories, the small refractive index of SiO_2 (n_{silica} = 1.45) provided large refractive index contrast between the epilayer and the substrate, contributing to more light extraction and higher outcoupling efficiency compared to the PSS.

Various nanoporous substrates for LEDs have been developed as advancements from conventional patterned sapphire substrates.[270–272] Zhou *et al.* introduced Ni nanodots on the PSS and fabricated nano–micro complex

patterned sapphire substrates (NMCPSS) by inductively coupled plasma (ICP) etching.[273] As shown in the SEM image (Fig. 10c), nanoscale cones derived from the Ni nanodots as the mask are densely formed on the microscale cones, making the substrate rougher. The light output power of the NMCPSS-based LED was 28.6% higher than that of the PSS-based LED. Through simulations, it was revealed that the enhancement was attributed to improved light extraction efficiency. Similarly, Cheng *et al.* fabricated a micro–nano patterned sapphire substrate (MNPSS) by using Ni nanoislands and ICP etching, as shown in Fig. 10d.[274] 3-Dimensional finite-difference time-domain simulation showed that the light extraction efficiency was 63% higher than that of the micropatterned sapphire substrate. Ke *et al.* prepared a hybrid patterned sapphire substrate (hybrid-PSS) by using an AAO etching mask.[275] An Al–Ti film deposited by e-beam evaporation on the microscale PSS was anodized to form the AAO layer with nanopatterns. The PSS was etched by ICP with the nanopatterned AAO layer as the mask, and nanopatterns were intricately formed on the microcones (Fig. 10e). The increased contact area between the LED and hybrid-PSS induced light scattering and increased the LED's view angle of 15°, enhancing the injection current.

Nanoporous oxides can also facilitate the efficient transport and injection of charge carriers within the LEDs. The porous structure can provide a larger surface area for contact between the active area and the electrodes, enabling better charge injection and reducing energy losses.[276] Chen *et al.* introduced NiO_x as the hole injection layer for quantum dot LEDs (QLEDs).[277] The NiO_x film was easily fabricated by spin-coating and showed spongelike nanostructures. The larger surface area enhanced hole injection and lowered the turn-on voltage compared to the NiO_x thin film. ZnO is the representative material in the electron transport layer for QLEDs because of its high electron mobility and transmittance. Kirkwood *et al.* introduced ZnO nanoparticles as the electron transport layer.[278] Compared to conventional ZnO films, the ZnO nanoparticles exhibited enhanced electron mobility by tuning defect density. The QLEDs showed improved efficiency and operating time. In QLEDs, nanoporous oxides can also serve as a matrix for embedding quantum dots (QDs). They can provide a suitable host matrix for dispersing and aligning quantum dots, thereby improving the efficiency and color purity of QLEDs. Wang *et al.* introduced mesoporous silica as the host matrix for $CsPbBr_3$ perovskite QDs.[279] The $CsPbBr_3$ QDs with a pore size of 12–14 nm were embedded in the mesoporous silica. The well-dispersed QDs prevent ion exchange and increase stability. Nanoporous oxides can also be applied as antireflection coatings on the surface of LEDs. These coatings help to minimize the reflection of light at the interface between the LED and the surrounding environment. By reducing unwanted reflections, more light can escape from the LED and contribute to the desired output, resulting in improved performance. Kim *et al.* introduced ITO nanorods by oblique-angle deposition and incorporated the ITO antireflection coating onto a GaInN LED.[280] The GaInN LED with ITO antireflection exhibited a light extraction efficiency enhancement of 24.3% compared to the LED with conventional ITO.

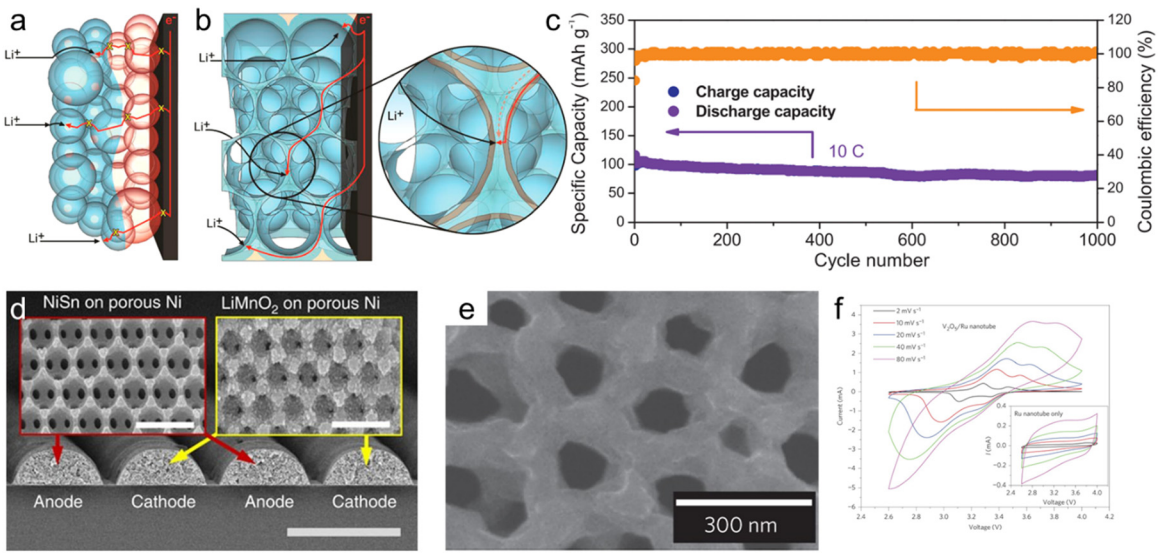

Fig. 11 Nanoporous oxide electrodes for batteries. Schematic comparing lithiation pathways for (a) nanoparticle and (b) 3DOM electrodes. Reproduced from ref. 287. Copyright 2016 Elsevier. (c) Cycling performance and coulombic efficiency of the $TiNb_2O_7$ anode at 10 C after 7 cycles at 0.1 C. Reproduced from ref. 290. Copyright 2017 Elsevier. d) Cross-sectional SEM images of the interdigitated electrodes spanning two periods. The insets show NiSn on the porous Ni anode and $LiMnO_2$ on the porous Ni cathode. Scale bars, 50 mm and 1 mm in the insets. Reproduced from ref. 136. Copyright 2013 Springer Nature. (e) SEM image of the device (top view), showing AAO pores remaining open after Ru and V_2O_5 ALD. (f) CVs of V_2O_5/Ru nanotubes and Ru nanotubes showing characteristic oxidation and reduction reaction peaks with scan rates up to 80 mV s^{-1}. Reproduced from ref. 292. Copyright 2014 Springer Nature.

4.2. Energy storage devices

4.2.1. Batteries. A battery is a representative energy storage device that converts chemical energy into electrical energy and *vice versa* through electrochemical oxidation/reduction reactions. Based on the faradaic charge storage mechanism, batteries provide high energy densities and are commonly used in various applications. Advancements in battery technology aim to improve energy density and cycle life, and various electrode materials are explored. Among them, nanoporous oxides offering high surface area enhance ion diffusion and increase active sites for reactions.[3,281] Although the typical intercalation-type electrodes based on 2D materials offer efficient charge transport pathways, their aggregation issue hinders the diffusion of ions.[282] On the other hand, 3DOM structures are promising electrode materials in terms of ion diffusion. Their interconnected pores create pathways for rapid metal ion flux, leading to faster charge and discharge rates.[283,284] The pores provide space for accommodating and storing ions, increasing the overall energy storage capacity of the battery.[285] In addition, the 3DOM structure can help accommodate the volume changes during charge and discharge cycles by providing room for expansion and contraction, reducing the strain on the electrode, and improving the cycle life of the battery.[286]

Lui *et al.* developed 3DOM TiO_2 electrodes as an anode in a Li-ion battery.[287] Fig. 11a and b show the comparison of lithiation pathways between the nanoparticle and 3DOM electrodes. In the nanoparticle electrodes, densely packed particles reduce the surface area contact with the electrolyte, and inside particles can be excluded from lithiation. Also, the movement of electrons in the nanoparticle electrode is limited to a specific path, and binding agents are required for high conductivity. On the other hand, in the 3DOM electrodes, the ordered pores offer high surface area contact with electrolytes, facilitating mass transport and complete lithiation. Also, the interconnected structures enhanced electron transport, and they can be manufactured without binding agents. The carbon-coated 3DOM TiO_2 electrode from polystyrene exhibited high-rate performance with a capacity of 174 mA h g^{-1} at 2 A g^{-1}. Also, the free volume in the 3DOM TiO_2 electrode contributes to the highly stable performance (181 mA h g^{-1}) with a capacity retention of 94.8% over 1000 cycles. Research on ternary nanoporous oxides for the electrodes of Li-ion batteries has also been conducted.[288,289] Lou *et al.* prepared a 3DOM $TiNbO_7$ anode with a high theoretical capacity of 387 mA h g^{-1}.[290] The honeycomb-like structure derived from the polystyrene crystal as a template offered a fast electron pathway and wide Li^+ insertion/extraction region. The 3DOM-$TiNb_2O_7$ anode recorded not only a remarkable rate capability of 120 mA h g^{-1} at 50 C but also durable long-term cyclability of 82% capacity retention over 1000 cycles at 10 C, as shown in Fig. 11c. Pikul *et al.* synthesized a 3DOM $LiMnO_2$ cathode on porous Ni and fabricated a Li-ion microbattery.[136] The 3DOM Ni framework was formed by electrodeposition onto polystyrene particles and etching of polystyrene. MnO_2 was electrodeposited on the 3DOM Ni framework and lithiated in molten salt. As shown in the cross-sectional SEM images (Fig. 11d), the NiSn anode and $LiMnO_2$ cathode were uniformly formed into the 3DOM structure following the Ni frameworks. The Li-ion microbattery delivered an energy density of 2.5 μW h cm^{-2} μm^{-1} at 0.5 C, showing a high power density of 7.4 mW cm^{-2} μm^{-1}, which is a comparable performance with supercapacitors. Similarly, Wang *et al.* fabricated a 3DOM Fe_2O_3 anode by using a Ni inverse opal as the support.[291] Due to the short electrode–electrolyte distances for electron and ion transport, the 3DOM Fe_2O_3 electrode exhibited excellent cycling and rate performances. Based on the enhanced kinetics, the electrode showed a

Table 2 Electrochemical performance of nanoporous oxide electrodes in energy storage devices

Batteries

Materials	Capacity [mA h g^{-1}]	Specific current	Cycling capacity [mA h g^{-1}]	Cycling [cls]	Ref.
3DOM TiO_2	174	2 A g^{-1}	181	1000	287
$ZnCo_2O_4$	932	1 A g^{-1}	932	50	289
3DOM $TiNbO_7$	387	1 C	120	1000	290
3DOM $LiMnO_2$	—	—	—	1000	136
3DOM Fe_2O_3	1000	0.2 A g^{-1}	400	100	291
V_2O_5/Ru NTs	80	150 C	80	1000	292

Supercapacitors

Materials	Specific capacitance [F g^{-1}]	Specific power density [W kg^{-1}]	Specific energy density [W h kg^{-1}]	Ref.
TArGO	372.1	—	—	302
RuO_2	50	—	—	305
RuO_2/CNT	644	17 000	4	5
MnO_2	144.1	1800	7.9	308
MnO_2/CNTs/MnO_2	341.5	—	—	309
Fe_2O_3/NPCTT	1846	7.48×10^{-4}	1.76×10^{-4}	310
$Ni(OH)_2$–MnO_2–rGO	1985	392	54	314
Co_3O_4	504	8000	36	315

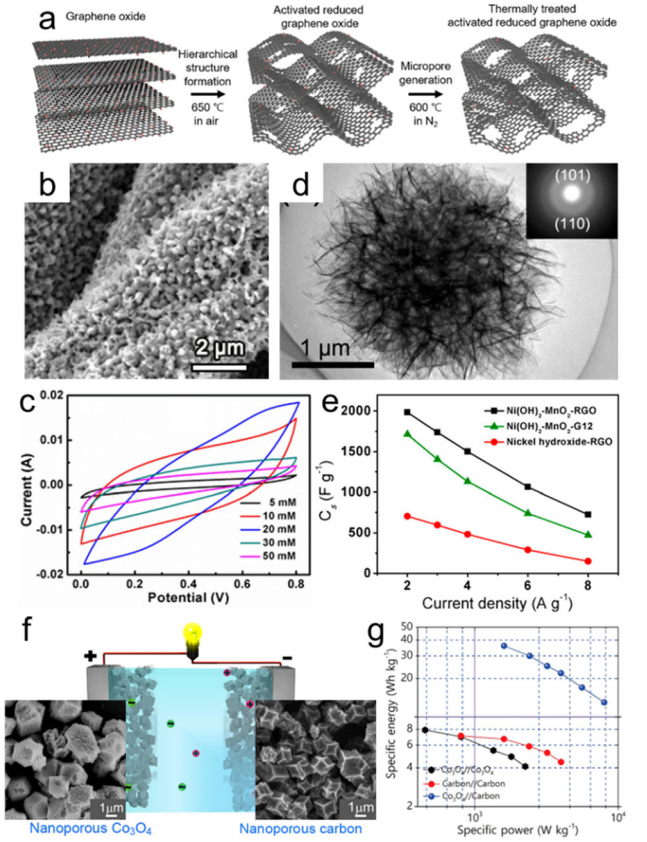

Fig. 12 Nanoporous oxide electrodes for supercapacitors. (a) Schematic for the preparation of thermally treated activated reduced graphene oxide (TArGO) powder. Reproduced from ref. 302. Copyright 2021 Springer Nature. (b) SEM image of the MnO/nanoporous carbon tube textile (NPCTT) product. (c) CV curves of MnO/NPCTT electrodes with different $C_{Fe^{3+}}$ at a scan rate of 10 mV s^{-1}. Reproduced from ref. 310. Copyright 2020 Springer Nature. (d) TEM image and (e) specific capacitance of the $Ni(OH)_2$–MnO_2–rGO hybrid sphere electrode. Reproduced from ref. 314. Copyright 2014 American Chemical Society. (f) Schematics of asymmetric supercapacitors (ASC) with nanoporous Co_3O_4 and nanoporous carbon as the positive and negative electrodes, respectively. (g) Ragone plots of SSCs and ASC based on nanoporous carbon and nanoporous Co_3O_4 electrodes. Reproduced from ref. 315. Copyright 2015 American Chemical Society.

specific capacity of 450 mA h g^{-1} and a reduced voltage hysteresis of 0.62 V at 0.1 A g^{-1}.

Liu *et al.* developed an all-in-one nanopore battery array derived from a self-assembled AAO template.[292] Each nanoelectrode was composed of a Ru nanotube current collector and V_2O_5 nanotube storage material, constructing a symmetric full nanopore battery array. The battery was asymmetrically cycled by forming the lithiated V_2O_5 anode and the pristine V_2O_5 cathode, as shown in the SEM image (Fig. 11e). In the CVs of the V_2O_5/Ru nanotubes (Fig. 11f), most of the reaction charge was used in the faradaic reaction process, indicating oxidation and reduction peaks. This means that the insertion of Li-ions took place quickly in the faradaic reaction, and these nanotube structures make the insertion of Li-ions comparable with fast double-layer charging. The nanopore battery array exhibited a high capacity of 80 mA h g^{-1} at 150 C with 80% retained capacity after 1000 cycles. We summarized the materials, capacities, and duration cycles of batteries in Table 2. While nanoporous oxide electrodes have shown potential in lithium-ion batteries, their application could extend beyond this. Research may focus on alternative energy storage systems, such as sodium-ion or potassium-ion batteries, where nanoporous oxide electrodes could exhibit superior performance and stability.

4.2.2. Supercapacitors. A supercapacitor is an energy storage device that stores and releases electrical energy through electrostatic double-layer capacitance (EDLC) or pseudocapacitance.[293] One of the key advantages of supercapacitors is their high power density, allowing them to charge and discharge rapidly. However, their energy density is lower compared to batteries, meaning that they store less energy per unit volume.[294] The challenge is to achieve a balance between high energy density and high power density, making supercapacitors a viable alternative to batteries in a wider range of applications. The high surface area of nanoporous oxides provides more sites for the adsorption and desorption of ions, enhancing the overall energy density of supercapacitors.[295–300] rGO is a widely studied and highly promising electrode material for supercapacitors.[301–303] It retains the excellent electrical conductivity of graphene, enabling efficient electron transport and reducing internal resistance within the electrode. Besides, it maintains a porous structure from the GO, allowing for high specific capacitance and improved charge storage capacity. Kim *et al.* tuned the hierarchical pore structures of GO with a two-step thermal annealing process (Fig. 12a).[302] At 650 °C in air, the oxygen-containing groups within the GO powder underwent decomposition into CO_x gases, causing the expansion of graphene sheets and the formation of porous structures. Subsequent thermal treatment of activated reduced GO (ArGO) at 600 °C in N_2 further reduced the remaining oxygen-containing groups, leading to an increased number of micropores (TArGO). The supercapacitor comprising TArGO indicated a high specific capacitance of 280 F g^{-1} at 1 A g^{-1} in 1 M H_2SO_4 with long-term stability after 10 000 cycle tests. The high EDLC was attributed to the high porosity of TArGO.

RuO_2 is one of the most efficient pseudocapacitive electrode materials.[304] It exhibits high specific capacitance and fast charge/discharge rates. Patake *et al.* synthesized nanoporous RuO_2 thin films for supercapacitors by chemical bath deposition. The large surface area of RuO_2 contributed to the high specific capacitance of 50 F g^{-1}.[305] Warren *et al.* coated highly active RuO_2 through atomic layer deposition on vertically aligned carbon nanotubes (CNTs) with extremely high porosity.[5] A further electrochemical oxidation process was carried out to achieve a specific capacitance of 644 F g^{-1} that is close to the theoretical value of RuO_2. MnO_2, which is cost-effective and exhibits high specific capacitance, is an excellent alternative to RuO_2.[306,307] Kumar *et al.* chemically synthesized hierarchical nanostructured MnO_2 for supercapacitors.[308] Also, Wang *et al.* encapsulated MnO_2 into

porous CNTs, and the optimal MnO_2/CNT/MnO_2 nanocomposites showed an excellent specific capacitance of 341.5 F g^{-1} and good rate performance.[309] This could be derived from the synergistic effect of MnO_2 with high-capacity storage and CNTs with high electrical conductivity. Ding *et al.* developed a facile synthesis method of non-noble metal oxides onto a nanoporous carbon tube textile (NPCTT) toward flexible supercapacitors.[310] The formation of nanostructures on the NPCTT was made possible through alkaline activation and infiltration of catalytic elements. As shown in Fig. 12b, MnO nanosheets were fabricated on the NPCTT without any aggregation, forming a porous and rough surface. This method was applied to the synthesis of hematite nanobelts, and the Fe_2O_3/NPCTT electrodes exhibited excellent flexibility with a high areal specific capacitance of 1846 mF cm^{-1} at 1 mA cm^{-2}, as shown in Fig. 12c.

There are various attempts to achieve excellent supercapacitor performances through the combination of metal oxides and carbon-based oxides.[311–313] Chen *et al.* reported $Ni(OH)_2$–MnO_2–rGO ternary hybrid sphere powders using a one-step hydrothermal method, as shown in Fig. 12d.[314] Although $Ni(OH)_2$ offers high capacitance and good cyclic stability, its relatively low electrical conductivity limits its performance. MnO_2 and rGO complement each other, and the synergistic effect and high specific surface area resulting from the nanoporous structure provide excellent characteristics that can replace noble metal oxides. The $Ni(OH)_2$–MnO_2–rGO ternary hybrid spheres showed a significantly improved specific capacitance of 1985 F g^{-1} and energy density of 54 W h kg^{-1} at 2 A g^{-1} compared to other composites, as shown in Fig. 12e. Salunkhe *et al.* synthesized two supercapacitor materials, nanoporous carbon, and nanoporous Co_3O_4, by varying the thermal treatment conditions from a single zeolite imidazolate framework (ZIF-67) precursor.[315] As shown in the SEM images (Fig. 12f), Co_3O_4 with a granular morphology offered a high surface area and good accessibility for ions, and nanoporous carbon also provided good electrical conductivity and a high surface area. Symmetric (SSC) and asymmetric supercapacitors (ASC) were fabricated using nanoporous carbon and Co_3O_4. The ASC recorded a high specific energy density of 36 W h kg^{-1} and a specific power density of 8000 W kg^{-1}, which were higher than those of the SSCs. We summarized the materials, specific capacitances, power densities, and energy densities in Table 2. Nanoporous oxide electrodes have played a crucial role in advancing energy storage solutions. Their high surface area and porous nature provided ample room for ion storage, leading to improved energy density and faster charging/discharging rates in supercapacitors. The application of nanoporous oxide electrodes could extend beyond this. Future developments might lead to the integration of nanoporous oxide electrodes into multifunctional energy devices. For instance, combining energy storage with energy conversion (like in hybrid supercapacitor–solar cell systems) could offer self-sustaining power solutions for various applications.

5. Summary and outlooks

Herein, we have systematically discussed the advances in structures, synthesis techniques, and applications of nanoporous oxides. Nanoporous oxide electrodes have demonstrated tremendous potential in various energy conversion and storage applications. Their dimensional diversity, from 0D to 3D, enables the construction of infinite nanoporous structures by controlling the pore size and morphology with the effective utilization of graphene oxides and binary, ternary, and multinary metal oxides. Various synthesis strategies, including bottom-up and top-down approaches, have allowed for the creation of elaborate nanoporous oxide electrodes. By exploiting the advantages derived from the structural characteristics of nanoporous oxides, such as enlarged surface area, efficient charge separation and transport, and the light trapping effect, they have exhibited superior properties in the field of energy conversion and storage. From fuel cells to supercapacitors, nanoporous oxides have been used as multifunctional electrodes, successfully overcoming major challenges in energy nanotechnologies. Although significant advances in the construction and applications of nanoporous oxide electrodes have been achieved in recent decades, there are still several challenges that need to be addressed to fully realize their potential.

First, it is important to carefully consider the performance degradation and stability issues associated with the increased surface area due to nanoporous structures. As mentioned above, the interconnected nanopore network enhances ion transport and accelerates the reaction rate; however, insufficient understanding of the flow dynamics within the nanoporous structure can adversely affect the reaction

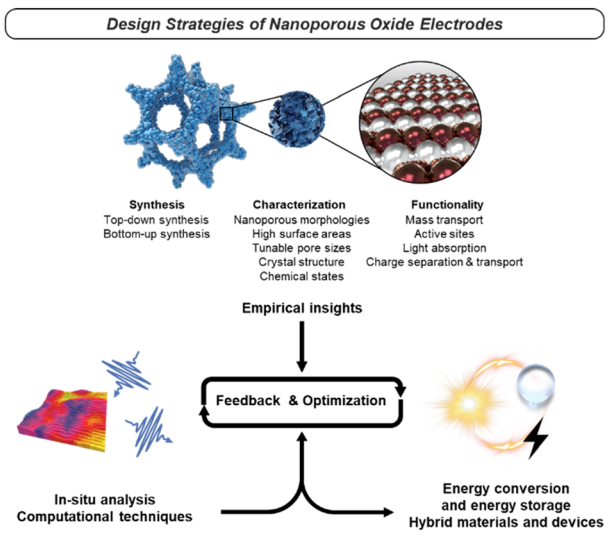

Fig. 13 Design strategies of nanoporous oxide electrodes.

kinetics. In addition, even though the reaction site is extended by increasing the surface area, it can also introduce detrimental surface trap sites, which can degrade performance and exacerbate stability issues. Therefore, to effectively harness the nanoporous geometry, it is essential to focus on real-time operating conditions. Specifically, computational modeling techniques, such as molecular dynamics simulations and computational fluid dynamics, and *in situ* analysis during operation are imperative approaches. This can provide rapid feedback to mitigate adverse effects in the actual reaction kinetics and contribute to the design of optimized nanoporous oxide structures tailored to real operational scenarios. Furthermore, to ensure stable and high-efficiency operation, a strategic approach is also needed in the synthesis aspect. A specific example of this strategy is the development of synthesis methods for oxide functional coatings that can conformally coat the complex surface of nanoporous oxides. Many previous studies have shown the effectiveness of such coatings in deactivating trap sites, and this approach should be further developed into a more universal method for conformally coating a wider range of functional oxides.

Second, the fabrication processes of nanoporous oxide electrodes need to be optimized to scale up the synthesis while maintaining cost-effectiveness. Synthesis methods that are difficult to obtain high yields and require complex steps are challenging to use practically. The problem of synthesizing nanoporous oxides uniformly while controlling the desired composition, shape, and surface conditions also poses a major obstacle. Therefore, synthesis strategies need to be improved in a direction that enhances high productivity and uniformity, suitable for the targeted applications. Specifically, it is necessary to approach the development of synthesis methods through computational-based predictions. To identify patterns and predict optimal synthesis conditions, machine learning models can be actively utilized using a dataset of both successful and unsuccessful attempts. Additionally, there are methodologies that involve implementing generative models like GANs (generative adversarial networks). These models can generate new synthesis recipes based on known data and iteratively optimize them. By implementing these specific solutions, researchers can harness the power of computational-based predictions to optimize the fabrication processes of nanoporous oxide electrodes more effectively, reducing the need for extensive trial-and-error experimentation.

Third, nanoporous oxides can enhance their value as effective electrodes in multiscale devices that integrate various energy nanotechnologies, going beyond the development of a single device. By effectively harnessing the electrical and chemical properties of oxide materials and incorporating nanoporous structures, performance and stability have reached a certain level. Following the development of a single device, effective integration of energy conversion and storage in hybrid devices will ultimately have a significant impact on the future energy industry. Nanoporous oxides, with their unique structural characteristics and tunable properties, hold high potential for widespread utilization in the design of such hybrid devices.

We present design strategies for the cyclic process of feedback and optimization, along with the current system and future directions (Fig. 13). To date, we have accumulated empirical data on numerous nanoporous oxide materials, spanning from their synthesis to material characterization, followed by functionality assessment. Our development strategy is anticipated to be grounded in the active utilization of *in situ* analysis and computational techniques. *In situ* analysis allows for meticulous observation of the operation of designed nanoporous oxide electrodes, enabling the acquisition of the most precise and reliable feedback. Furthermore, the proactive use of computational techniques can expand our understanding of materials, from the synthesis to operational conditions, encompassing insights from the material level to the system level. In a more advanced phase, we envision the prospects of designing devices that integrate energy conversion and storage, based on nanoporous oxide electrodes. Although research at the system level holds the promise of significantly enhancing energy cycles, the complexity of interconnecting multiple systems currently presents delays. In the future, we anticipate that the considerable advancements in individual applications of nanoporous oxide electrodes will converge to create opportunities for their utilization in integrated devices. These system-level studies, built upon the substantial progress in various applications of nanoporous oxide electrodes, are expected to pave the way for the development of novel devices with improved efficiency and enhanced capabilities.

Author contributions

Jin Wook Yang: conceptualization, investigation, visualization, writing (original draft, review & editing). Hee Ryeong Kwon: conceptualization, investigation, visualization, writing (original draft, review & editing). Jin Ho Seo: conceptualization, investigation, visualization, writing (original draft, review & editing). Sangwoo Ryu: supervision. Ho Won Jang: conceptualization, writing (review & editing), supervision, funding.

Conflicts of interest

There are no conflicts to declare.

Acknowledgements

This work was supported by the National Research Foundation of Korea (NRF) funded by the Korea government Ministry of Science and ICT (MSIT) (2021R1A2B5B03001851, 2021M3H4A1A03057403). This work was also supported by

the KRISS (Korea Research Institute of Standards and Science) MPI Lab. Program. Jin Wook Yang acknowledges the NRF funded by the Korea government MSIT (RS-2023-00213786). The Inter-University Semiconductor Research Center and Institute of Engineering Research at Seoul National University provided research facilities for this work.

Notes and references

1 T. Y. Ma, S. Dai, M. Jaroniec and S. Z. Qiao, *J. Am. Chem. Soc.*, 2014, **136**, 13925–13931.
2 C. W. Kwon, J. W. Son, J. H. Lee, H. M. Kim, H. W. Lee and K. B. Kim, *Adv. Funct. Mater.*, 2011, **21**, 1154–1159.
3 N. Liu, H. Ma, L. Wang, Y. Zhao, Z. Bakenov and X. Wang, *J. Mater. Sci. Technol.*, 2021, **84**, 124–132.
4 D. Lei, D. C. Lee, E. Zhao, A. Magasinski, H. R. Jung, G. Berdichevsky, D. Steingart and G. Yushin, *Nano Energy*, 2018, **48**, 170–179.
5 R. Warren, F. Sammoura, F. Tounsi, M. Sanghadasa and L. Lin, *J. Mater. Chem. A*, 2015, **3**, 15568–15575.
6 N. Ogihara, Y. Itou, T. Sasaki and Y. Takeuchi, *J. Phys. Chem. C*, 2015, **119**, 4612–4619.
7 J. An, Y. B. Kim, J. Park, T. M. Gür and F. B. Prinz, *Nano Lett.*, 2013, **13**, 4551–4555.
8 H. Lee, J. W. Yang, J. Tan, J. Park, S. G. Shim, Y. S. Park, J. Yun, K. Kim, H. W. Jang and J. Moon, *Adv. Sci.*, 2021, **8**, 2102458.
9 S. M. H. Hejazi, J. Aghazadeh Mohandesi and M. Javanbakht, *Sol. Energy*, 2017, **144**, 699–706.
10 J. H. Son, J. U. Kim, Y. H. Song, B. J. Kim, C. J. Ryu and J. L. Lee, *Adv. Mater.*, 2012, **24**, 2259–2262.
11 H. Yu, W. Wang, M. Liu, T. Zhao, R. Lin, M. Hou, Y. Kou, L. Chen, A. A. Elzatahry, F. Zhang, D. Zhao and X. Li, *Sci. Adv.*, 2022, **8**, eabq2356.
12 M. Thommes, K. Kaneko, A. V. Neimark, J. P. Olivier, F. Rodriguez-Reinoso, J. Rouquerol and K. S. W. Sing, *Pure Appl. Chem.*, 2015, **87**, 1051–1069.
13 J. Li, X. Jin, R. Li, Y. Zhao, X. Wang, X. Liu and H. Jiao, *Appl. Catal., B*, 2019, **240**, 1–8.
14 T. A. Knecht and J. E. Hutchison, *Chem. Mater.*, 2023, **35**, 3151–3161.
15 M. Košiček, J. Zavašnik, O. Baranov, B. Šetina Batič and U. Cvelbar, *Cryst. Growth Des.*, 2022, **22**, 6656–6666.
16 N. Du, H. Zhang, B. Chen, M. Xiangyang, Z. Liu, J. Wu and D. Yang, *Adv. Mater.*, 2007, **19**, 1641–1645.
17 J. Zhu, Z. Yin, H. Li, H. Tan, C. L. Chow, H. Zhang, H. H. Hng, J. Ma and Q. Yan, *Small*, 2011, **7**, 3458–3464.
18 X. Yu, T. J. Marks and A. Facchetti, *Nat. Mater.*, 2016, **15**, 383–396.
19 Z. Yu, H. Liu, M. Zhu, Y. Li and W. Li, *Small*, 2021, **17**, 1903378.
20 T. Liu, Y. Qu, J. Liu, L. Zhang, B. Cheng and J. Yu, *Small*, 2021, **17**, 2103673.
21 G. Y. Yoo, N. Nurrosyid, S. Lee, Y. Jeong, I. Yoon, C. Kim, W. Kim, S. Y. Jang and Y. R. Do, *ACS Appl. Mater. Interfaces*, 2020, **12**, 10626–10636.
22 C. W. Chen, H. W. Tsai, Y. C. Wang, Y. C. Shih, T. Y. Su, C. H. Yang, W. S. Lin, C. H. Shen, J. M. Shieh and Y. L. Chueh, *Adv. Funct. Mater.*, 2019, **29**, 1905040.
23 C. Sun, J. A. Alonso and J. Bian, *Adv. Energy Mater.*, 2021, **11**, 2000459.
24 J. W. Choi and D. Aurbach, *Nat. Rev. Mater.*, 2016, **1**, 16013.
25 W. Yu, L. Sisi, Y. Haiyan and L. Jie, *RSC Adv.*, 2020, **10**, 15328–15345.
26 T. Hirano, S. Kaseda, C. Kiet Le Anh, F. Iskandar, E. Tanabe and T. Ogi, *ACS Appl. Nano Mater.*, 2022, **5**, 15449–15456.
27 M. Liu, H. Xia, W. Yang, X. Liu, J. Xiang, X. Wang, L. Hu and F. Lu, *Appl. Catal., B*, 2022, **301**, 120765.
28 L. Li, J. Yan, T. Wang, Z. J. Zhao, J. Zhang, J. Gong and N. Guan, *Nat. Commun.*, 2015, **6**, 5881.
29 J. Park, J. Joo, G. K. Soon, Y. Jang and T. Hyeon, *Angew. Chem., Int. Ed.*, 2007, **46**, 4630–4660.
30 P. Wainer, O. Kendall, A. Lamb, S. J. Barrow, A. Tricoli, D. E. Gómez, J. Van Embden and E. Della Gaspera, *Chem. Mater.*, 2019, **31**, 9604–9613.
31 L. Sang, Y. Zhao and C. Burda, *Chem. Rev.*, 2014, **114**, 9283–9318.
32 Z. Zhu, Y. Bai, X. Liu, C. C. Chueh, S. Yang and A. K. Y. Jen, *Adv. Mater.*, 2016, **28**, 6478–6484.
33 H. M. Jeong, K. M. Choi, T. Cheng, D. K. Lee, R. Zhou, I. W. Ock, D. J. Milliron, W. A. Goddard and J. K. Kang, *Proc. Natl. Acad. Sci. U. S. A.*, 2015, **112**, 7914–7919.
34 X. Chen, L. L. Yu and S. S. Mao, *Science*, 2011, **331**, 746–750.
35 J. Klein, M. Philippi, F. Alarslan, T. Jähnichen, D. Enke, M. Steinhart and M. Haase, *Small*, 2023, **19**, 2207674.
36 S. Cong, Y. Tian, Q. Li, Z. Zhao and F. Geng, *Adv. Mater.*, 2014, **26**, 4260–4267.
37 H. Xia, C. Hong, B. Li, B. Zhao, Z. Lin, M. Zheng, S. V. Savilov and S. M. Aldoshin, *Adv. Funct. Mater.*, 2015, **25**, 627–635.
38 M. Ye, Z. Zhao, Z. Hu, L. Liu, H. Ji, Z. Shen and T. Ma, *Angew. Chem.*, 2017, **129**, 8527–8531.
39 S. Sun, H. Zeng, D. B. Robinson, S. Raoux, P. M. Rice, S. X. Wang and G. Li, *J. Am. Chem. Soc.*, 2004, **126**, 273–279.
40 J. Ahn, Y. Song, Y. J. Kim, D. Nam, T. Kim, K. Kwak, C. Hoon Kwon, Y. Ko, S. J. Lee and J. Cho, *Chem. Eng. J.*, 2023, **455**, 140742.
41 M. Xiao, Z. Wang, M. Lyu, B. Luo, S. Wang, G. Liu, H. M. Cheng and L. Wang, *Adv. Mater.*, 2019, **31**, 1801369.
42 B. Koo, H. Xiong, M. D. Slater, V. B. Prakapenka, M. Balasubramanian, P. Podsiadlo, C. S. Johnson, T. Rajh and E. V. Shevchenko, *Nano Lett.*, 2012, **12**, 2429–2435.
43 Z. Yan, W. Huang, X. Jiang, J. Gao, Y. Hu, H. Zhang and Q. Shi, *Microporous Mesoporous Mater.*, 2021, **323**, 111228.
44 S. H. Hwang, J. Yun and J. Jang, *Adv. Funct. Mater.*, 2014, **24**, 7619–7626.
45 S. Li, J. Niu, Y. C. Zhao, K. P. So, C. Wang, C. A. Wang and J. Li, *Nat. Commun.*, 2015, **6**, 7872.
46 M. Zhou, T. Wang, Z. He, Y. Xu, W. Yu, B. Shi and K. Huang, *ACS Sustainable Chem. Eng.*, 2019, **7**, 2924–2932.

47 N. Jiang, D. Li, L. Liang, Q. Xu, L. Shao, S. Bin Wang, A. Chen and J. Wang, *Nano Res.*, 2020, **13**, 1354–1362.
48 Q. Wei, F. Xiong, S. Tan, L. Huang, E. H. Lan, B. Dunn and L. Mai, *Adv. Mater.*, 2017, **29**, 1602300.
49 I. Hussain, T. Mak and K. Zhang, *ACS Appl. Nano Mater.*, 2021, **4**, 129–141.
50 R. Venkatesan, R. Bauri and K. K. Mayuranathan, *Energy Fuels*, 2022, **36**, 7854–7864.
51 H. Jin Han, G. Rac Lee, Y. Xie, H. Jang, D. J. Hynek, E. N. Cho, Y. Ji Kim, Y. S. Jung and J. J. Cha, *Sci. Adv.*, 2021, **7**, eabh2012.
52 X. Li and J. Wang, *InfoMat*, 2020, **2**, 3–32.
53 B. Liu and E. S. Aydil, *J. Am. Chem. Soc.*, 2009, **131**, 3985–3990.
54 Y. Xing, X. Sheng, H. Zhou, D. Wang, X. Chen and X. Feng, *J. Phys. Chem. C*, 2022, **126**, 1966–1971.
55 P. Zhang, Z. Tian, Y. Kang, B. He, Z. Zhao, C. Te Hung, L. Duan, W. Chen, Y. Tang, J. Yu, L. Mai, Y. F. Li, W. Li and D. Zhao, *J. Am. Chem. Soc.*, 2022, **144**, 20964–20974.
56 N. C. Hildebrandt, J. Soldat and R. Marschall, *Small*, 2015, **11**, 2051–2057.
57 L. Tian, Z. Zhang, S. Liu, G. Li and X. Gao, *Energy Environ. Mater.*, 2022, **5**, 645–654.
58 P. Roy, S. Berger and P. Schmuki, *Angew. Chem., Int. Ed.*, 2011, **50**, 2904–2939.
59 C. Niu, J. Meng, X. Wang, C. Han, M. Yan, K. Zhao, X. Xu, W. Ren, Y. Zhao, L. Xu, Q. Zhang, D. Zhao and L. Mai, *Nat. Commun.*, 2015, **6**, 7402.
60 Y. Lei, Q. Wang, S. Peng, S. Ramakrishna, D. Zhang and K. Zhou, *Adv. Energy Mater.*, 2020, **10**, 1902115.
61 S. Peng, L. Li, Y. Hu, M. Srinivasan, F. Cheng, J. Chen and S. Ramakrishna, *ACS Nano*, 2015, **9**, 1945–1954.
62 H. Wang, X. Liu, P. Niu, S. Wang, J. Shi and L. Li, *Matter*, 2020, **2**, 1377–1413.
63 H. Xie, Z. Li, L. Cheng, A. A. Haidry, J. Tao, Y. Xu, K. Xu and J. Z. Ou, *iScience*, 2022, **25**, 103598.
64 Y. Tian, Z. Yu, L. Cao, X. L. Zhang, C. Sun and D. W. Wang, *J. Energy Chem.*, 2021, **55**, 323–344.
65 L. Mao, H. Park, R. A. Soler-Crespo, H. D. Espinosa, T. H. Han, S. B. T. Nguyen and J. Huang, *Nat. Commun.*, 2019, **10**, 3677.
66 J. Li, J. Lv, Y. C. Hao, L. W. Chen, Y. Zuo, Y. Liu, S. Li, F. Zhang, F. Deng, A. X. Yin, J. Zhou, P. Li and B. Wang, *ACS Appl. Mater. Interfaces*, 2021, **13**, 47478–47487.
67 H. Kaur and J. N. Coleman, *Adv. Mater.*, 2022, **34**, 2202164.
68 A. Puthirath Balan, S. Radhakrishnan, C. F. Woellner, S. K. Sinha, L. Deng, C. D. L. Reyes, B. M. Rao, M. Paulose, R. Neupane, A. Apte, V. Kochat, R. Vajtai, A. R. Harutyunyan, C. W. Chu, G. Costin, D. S. Galvao, A. A. Martí, P. A. Van Aken, O. K. Varghese, C. S. Tiwary, A. M. M. R. Iyer and P. M. Ajayan, *Nat. Nanotechnol.*, 2018, **13**, 602–609.
69 L. Lin, N. Xu, C. Wu, J. Huang, A. Nattestad, X. Zheng, G. G. Wallace, S. Zhang and J. Chen, *Matter*, 2021, **4**, 955–968.
70 Z. Sun, T. Liao, Y. Dou, S. M. Hwang, M. S. Park, L. Jiang, J. H. Kim and S. X. Dou, *Nat. Commun.*, 2014, **5**, 3813.
71 L. Peng, P. Xiong, L. Ma, Y. Yuan, Y. Zhu, D. Chen, X. Luo, J. Lu, K. Amine and G. Yu, *Nat. Commun.*, 2017, **8**, 15139.
72 K. Liu, H. Jin, L. Huang, Y. Luo, Z. Zhu, S. Dai, X. Zhuang, Z. Wang, L. Huang and J. Zhou, *Sci. Adv.*, 2022, **8**, eabn2030.
73 W. Q. Wu, Y. F. Xu, J. F. Liao, L. Wang and D. Bin Kuang, *Nano Energy*, 2019, **62**, 791–809.
74 H. Liao, X. Guo, Y. Hou, H. Liang, Z. Zhou and H. Yang, *Small*, 2020, **16**, 1905223.
75 C. O'Dwyer, D. Navas, V. Lavayen, E. Benavente, M. A. Santa Ana, G. González, S. B. Newcomb and C. M. Sotomayor Torres, *Chem. Mater.*, 2006, **18**, 3016–3022.
76 W. Q. Wu, H. L. Feng, H. S. Rao, Y. F. Xu, D. Bin Kuang and C. Y. Su, *Nat. Commun.*, 2014, **5**, 3968.
77 J. H. Kim, D. H. Kim, J. W. Yoon, Z. Dai and J. H. Lee, *ACS Appl. Energy Mater.*, 2019, **2**, 4535–4543.
78 S. H. Ko, D. Lee, H. W. Kang, K. H. Nam, J. Y. Yeo, S. J. Hong, C. P. Grigoropoulos and H. J. Sung, *Nano Lett.*, 2011, **11**, 666–671.
79 X. Gu, L. Chen, Z. Ju, H. Xu, J. Yang and Y. Qian, *Adv. Funct. Mater.*, 2013, **23**, 4049–4056.
80 U. Shaislamov, K. Krishnamoorthy, S. J. Kim, A. Abidov, B. Allabergenov, S. Kim, S. Choi, R. Suresh, W. M. Ahmed and H. J. Lee, *Int. J. Hydrogen Energy*, 2016, **41**, 2253–2262.
81 Y. Ouyang, R. Huang, X. Xia, H. Ye, X. Jiao, L. Wang, W. Lei and Q. Hao, *Chem. Eng. J.*, 2019, **355**, 416–427.
82 Z. Hao, Z. Meng, X. Li, X. Sun, J. Xu, H. Nan, W. Shi, G. Qi, X. Hu and H. Tian, *J. Colloid Interface Sci.*, 2022, **617**, 430–441.
83 Z. Sun, J. H. Kim, Y. Zhao, F. Bijarbooneh, V. Malgras, Y. Lee, Y. M. Kang and S. X. Dou, *J. Am. Chem. Soc.*, 2011, **133**, 19314–19317.
84 Y. C. Tsai, N. Nhat Huy, J. Lee, Y. F. Lin and K. Y. A. Lin, *Chem. Eng. J.*, 2020, **395**, 124939.
85 K. Jing, W. Ma, Y. Ren, J. Xiong, B. Guo, Y. Song, S. Liang and L. Wu, *Appl. Catal., B*, 2019, **243**, 10–18.
86 Y. T. Kim, P. P. Lopes, S. A. Park, A. Y. Lee, J. Lim, H. Lee, S. Back, Y. Jung, N. Danilovic, V. Stamenkovic, J. Erlebacher, J. Snyder and N. M. Markovic, *Nat. Commun.*, 2017, **8**, 1449.
87 T. K. Kim, K. J. Lee, J. Y. Cheon, J. H. Lee, S. H. Joo and H. R. Moon, *J. Am. Chem. Soc.*, 2013, **135**, 8940–8946.
88 X. Yan, W. Liu, H. Kang, S. Zhang and S. Shi, *Adv. Funct. Mater.*, 2023, **33**, 2212654.
89 X. Tan, L. Guo, S. Liu, J. Wu, T. Zhao, J. Ren, Y. Liu, X. Kang, H. Wang, L. Sun and W. Chu, *Adv. Funct. Mater.*, 2019, **29**, 1903003.
90 C. Wang, M. Wang, L. Liu and Y. Huang, *ACS Appl. Energy Mater.*, 2021, **4**, 1833–1839.
91 J. Hwang, C. Jo, K. Hur, J. Lim, S. Kim and J. Lee, *J. Am. Chem. Soc.*, 2014, **136**, 16066–16072.
92 J. E. S. Van Der Hoeven, A. V. Shneidman, N. J. Nicolas and J. Aizenberg, *Acc. Chem. Res.*, 2022, **55**, 1809–1820.
93 B. T. Liu, X. M. Shi, X. Y. Lang, L. Gu, Z. Wen, M. Zhao and Q. Jiang, *Nat. Commun.*, 2018, **9**, 1375.
94 D. McNulty, E. Carroll and C. O'Dwyer, *Adv. Energy Mater.*, 2017, **7**, 1602291.

95 Y. Wang, H. Arandiyan, H. A. Tahini, J. Scott, X. Tan, H. Dai, J. D. Gale, A. L. Rohl, S. C. Smith and R. Amal, *Nat. Commun.*, 2017, **8**, 15553.
96 X. Fan, Y. Liu, S. Chen, J. Shi, J. Wang, A. Fan, W. Zan, S. Li, W. A. Goddard and X. M. Zhang, *Nat. Commun.*, 2018, **9**, 1809.
97 H. Zhang, X. Yu and P. V. Braun, *Nat. Nanotechnol.*, 2011, **6**, 277–281.
98 Y. Jiang, J. L. Yue, Q. Guo, Q. Xia, C. Zhou, T. Feng, J. Xu and H. Xia, *Small*, 2018, **14**, 1704296.
99 J. Deng, Y. Su, D. Liu, P. Yang, B. Liu and C. Liu, *Chem. Rev.*, 2019, **119**, 9221–9259.
100 J. Cai and L. Qi, *Mater. Horiz.*, 2015, **2**, 37–53.
101 E. Larson, L. Williams, C. Jin, X. Chen, J. DiCesare, O. Sheppard, S. Xu and J. Wu, *J. Mater. Res.*, 2022, **37**, 2204–2215.
102 T. K. Das, P. Ilaiyaraja and C. Sudakar, *Sol. Energy*, 2018, **159**, 920–929.
103 M. H. Habibi, A. H. Habibi, M. Zendehdel and M. Habibi, *Spectrochim. Acta, Part A*, 2013, **110**, 226–232.
104 M. H. Habibi, E. Askari, M. Habibi and M. Zendehdel, *Spectrochim. Acta, Part A*, 2013, **104**, 197–202.
105 Y. J. Kim, M. H. Lee, H. J. Kim, G. Lim, Y. S. Choi, N. G. Park, K. Kim and W. I. Lee, *Adv. Mater.*, 2009, **21**, 3668–3673.
106 T. Azizi, A. E. Touihri, M. Ben Karoui and R. Gharbi, *Optik*, 2016, **127**, 4400–4404.
107 M. Ben Karoui, S. Saadaoui, A. Torchani and R. Gharbi, *J. Electron. Mater.*, 2021, **50**, 4797–4805.
108 I. G. Yu, Y. J. Kim, H. J. Kim, C. Lee and W. I. Lee, *J. Mater. Chem.*, 2011, **21**, 532–538.
109 Z. Tebby, T. Uddin, Y. Nicolas, C. Olivier, T. Toupance, C. Labrugère and L. Hirsch, *ACS Appl. Mater. Interfaces*, 2011, **3**, 1485–1491.
110 P. K. Singh, B. Bhattacharya and R. K. Nagarale, *J. Appl. Polym. Sci.*, 2010, **118**, 2976–2980.
111 H. J. Kim, J. K. Seo, Y. J. Kim, H. K. Jeong, G. Il Lim, Y. S. Choi and W. I. Lee, *Sol. Energy Mater. Sol. Cells*, 2009, **93**, 2108–2112.
112 Z. Tebby, O. Babot, T. Toupance, D. H. Park, G. Campet and M. H. Delville, *Chem. Mater.*, 2008, **20**, 7260–7267.
113 N. Nang Dinh, N. Minh Quyen, D. N. Chung, M. Zikova and V. Van Truong, *Sol. Energy Mater. Sol. Cells*, 2011, **95**, 618–623.
114 S. Sharma, A. M. Volosin, D. Schmitt and D. K. Seo, *J. Mater. Chem. A*, 2013, **1**, 699–706.
115 H. V. Le, P. T. Pham, L. T. Le, A. D. Nguyen, N. Q. Tran and P. D. Tran, *Int. J. Hydrogen Energy*, 2021, **46**, 22852–22863.
116 X. Zhang, D. Chandra, M. Kajita, H. Takahashi, L. Dong, A. Shoji, K. Saito, T. Yui and M. Yagi, *Int. J. Hydrogen Energy*, 2014, **39**, 20736–20743.
117 D. Frederichi, M. H. N. O. Scaliante and R. Bergamasco, *Environ. Sci. Pollut. Res.*, 2021, **28**, 23610–23633.
118 J. Zhao, Z. Tao, J. Liang and J. Chen, *Cryst. Growth Des.*, 2008, **8**, 2799–2805.
119 X. Jiang, F. Cai, D. Gao, J. Dong, S. Miao, G. Wang and X. Bao, *Electrochem. Commun.*, 2016, **68**, 67–70.
120 K. Nguyen, N. D. Hoa, C. M. Hung, D. T. Thanh Le, N. Van Duy and N. Van Hieu, *RSC Adv.*, 2018, **8**, 19449–19455.
121 P. S. Bassi, S. Y. Chiam, Gurudayal, J. Barber and L. H. Wong, *ACS Appl. Mater. Interfaces*, 2014, **6**, 22490–22495.
122 J. Lv and T. Liang, *Chem. Phys. Lett.*, 2016, **659**, 61–65.
123 G. Wang, X. Shen, J. Horvat, B. Wang, H. Liu, D. Wexler and J. Yao, *J. Phys. Chem. C*, 2009, **113**, 4357–4361.
124 Q. Abbas, S. H. Siyal, A. Mateen, N. U. Hassan, A. Idrees, Z. U. Rehman, E. M. T. El Din, M. A. Bajaber and M. S. Javed, *Materials*, 2022, **15**, 4499.
125 F. Yang, X. Zhang, Y. Yang, S. Hao and L. Cui, *Chem. Phys. Lett.*, 2018, **691**, 366–372.
126 S. K. Meher, P. Justin and G. R. Rao, *Electrochim. Acta*, 2010, **55**, 8388–8396.
127 R. Ahmad and M. A. Shah, *Ceram. Int.*, 2023, **49**, 6470–6478.
128 G. Rajamanickam, S. Narendhiran, S. P. Muthu, S. Mukhopadhyay and R. Perumalsamy, *Chem. Phys. Lett.*, 2017, **689**, 19–25.
129 T. Xu, H. Zheng, P. Zhang, W. Lin and Y. Sekiguchi, *J. Mater. Chem. A*, 2015, **3**, 19115–19122.
130 A. Manimekalai, P. Vivek, M. Manupriya, M. Umadevi and R. Parimaladevi, *Surf. Interfaces*, 2023, **41**, 103176.
131 Y. E. Firat and A. Peksoz, *J. Mater. Sci.*, 2017, **28**, 3515–3522.
132 M. S. Wu, Y. A. Huang, C. H. Yang and J. J. Jow, *Int. J. Hydrogen Energy*, 2007, **32**, 4153–4159.
133 S. M. Pawar, B. S. Pawar, P. T. Babar, A. T. A. Ahmed, H. S. Chavan, Y. Jo, S. Cho, J. Kim, B. Hou, A. I. Inamdar, S. N. Cha, J. H. Kim, T. G. Kim, H. Kim and H. Im, *Appl. Surf. Sci.*, 2019, **470**, 360–367.
134 H. Shen, X. Yang, J. Song, H. Gao, Z. Wu, J. Yu, W. Lei, J. Yang, G. He and Q. Hao, *J. Solid State Electrochem.*, 2022, **26**, 353–363.
135 X. He, Z. He, Q. Zou and L. Wu, *Int. J. Energy Res.*, 2020, **44**, 2100–2109.
136 J. H. Pikul, H. Gang Zhang, J. Cho, P. V. Braun and W. P. King, *Nat. Commun.*, 2013, **4**, 1732.
137 C. Dunkel, M. Wark, T. Oekermann, R. Ostermann and B. M. Smarsly, *Electrochim. Acta*, 2013, **90**, 375–381.
138 A. Y. El-Etre and S. M. Reda, *Appl. Surf. Sci.*, 2010, **256**, 6601–6606.
139 Z. Chen, Y. Tang, L. Zhang and L. Luo, *Electrochim. Acta*, 2006, **51**, 5870–5875.
140 G. P. Wheeler and K. S. Choi, *ACS Energy Lett.*, 2017, **2**, 2378–2382.
141 H. Razmi and R. Mohammad-Rezaei, *Electrochim. Acta*, 2011, **56**, 7220–7223.
142 K. R. Tolod, S. Hernández, M. Castellino, F. A. Deorsola, E. Davarpanah and N. Russo, *Int. J. Hydrogen Energy*, 2020, **45**, 605–618.
143 D. P. Ura and U. Stachewicz, *Macromol. Mater. Eng.*, 2022, **307**, 2100843.
144 W. Luo, X. Hu, Y. Sun and Y. Huang, *J. Mater. Chem.*, 2012, **22**, 8916–8921.
145 M. Kundu and L. Liu, *J. Nanosci. Lett.*, 2015, **5**, 11.

146 Z. Yang, G. Du, C. Feng, S. Li, Z. Chen, P. Zhang, Z. Guo, X. Yu, G. Chen, S. Huang and H. Liu, *Electrochim. Acta*, 2010, **55**, 5485–5491.
147 L. Qiao, X. Wang, X. Sun, X. Li, Y. Zheng and D. He, *Nanoscale*, 2013, **5**, 3037–3042.
148 X. Zhao, L. Jiang, C. Ma, L. Cheng, C. Wang, G. Chen, H. Yue and D. Zhang, *J. Power Sources*, 2021, **490**, 229534.
149 L. Thirugunanam, S. Kaveri, V. Etacheri, S. Ramaprabhu, M. Dutta and V. G. Pol, *Mater. Charact.*, 2017, **131**, 64–71.
150 Z. Zhou, W. Xiao, X. Shi, B. Ding, Q. Wang, Y. Zhan, H. Deng and Y. Du, *J. Colloid Interface Sci.*, 2017, **490**, 74–83.
151 Y. Yang, J. Zhu, W. Shi, J. Zhou, D. Gong, S. Gu, L. Wang, Z. Xu and B. Lu, *Mater. Lett.*, 2016, **177**, 34–38.
152 Y. Lu, Y. Liu, J. Mo, B. Deng, J. Wang, Y. Zhu, X. Xiao and G. Xu, *J. Alloys Compd.*, 2021, **853**, 157271.
153 R. R. Poolakkandy and M. M. Menamparambath, *Nanoscale Adv.*, 2020, **2**, 5015–5045.
154 K. J. Hwang, D. W. Cho, J. W. Lee and C. Im, *New J. Chem.*, 2012, **36**, 2094–2100.
155 Y. Lee and M. Kang, *Mater. Chem. Phys.*, 2010, **122**, 284–289.
156 S. E. Moosavifard, J. Shamsi and M. Ayazpour, *Ceram. Int.*, 2015, **41**, 1831–1837.
157 S. E. Moosavifard, M. F. El-Kady, M. S. Rahmanifar, R. B. Kaner and M. F. Mousavi, *ACS Appl. Mater. Interfaces*, 2015, **7**, 4851–4860.
158 S. E. Moosavifard, J. Shamsi, S. Fani and S. Kadkhodazade, *RSC Adv.*, 2014, **4**, 52555–52561.
159 A. Fadhli, D. Erika, S. Mardiana, C. B. Rasrendra, M. Khalil and G. T. M. Kadja, *Chem. Phys. Lett.*, 2022, **803**, 139809.
160 N. J. Carroll, P. F. Crowder, S. Pylypenko, W. Patterson, D. R. Ratnaweera, D. Perahia, P. Atanassov and D. N. Petsev, *ACS Appl. Mater. Interfaces*, 2013, **5**, 3524–3529.
161 Z. Liu, Y. Li, Z. Zhao, Y. Cui, K. Hara and M. Miyauchi, *J. Mater. Chem.*, 2010, **20**, 492–497.
162 R. Z. Hou, P. Ferreira and P. M. Vilarinho, *Chem. Mater.*, 2009, **21**, 3536–3541.
163 W. Jiang, C. Jiang, X. Gong and Z. Zhang, *J. Sol-Gel Sci. Technol.*, 2009, **52**, 8–14.
164 D. Feng, T. N. Gao, L. Zhang, B. Guo, S. Song, Z. A. Qiao and S. Dai, *Nano-Micro Lett.*, 2020, **12**, 14.
165 F. Jonas, B. Lebeau, S. Siffert, L. Michelin, C. Poupin, R. Cousin, L. Josien, L. Vidal, M. Mallet, P. Gaudin and J. L. Blin, *ACS Appl. Nano Mater.*, 2021, **4**, 1786–1797.
166 W. Wei, P. Du, D. Liu, H. Wang and P. Liu, *J. Colloid Interface Sci.*, 2017, **503**, 205–213.
167 M. R. Krishnan, V. Rajendran and E. Alsharaeh, *J. Non-Cryst. Solids*, 2023, **606**, 122198.
168 M. S. Seo, I. Jeong, J. S. Park, J. Lee, I. K. Han, W. I. Lee, H. J. Son, B. H. Sohn and M. J. Ko, *Nanoscale*, 2016, **8**, 11472–11479.
169 Y. Zhang, J. Li, F. Kang, F. Gao and X. Wang, *Int. J. Hydrogen Energy*, 2012, **37**, 860–866.
170 S. H. Kim, B. Y. H. Liu and M. R. Zachariah, *Chem. Mater.*, 2002, **14**, 2889–2899.
171 A. A. Yadav, T. B. Deshmukh, R. V. Deshmukh, D. D. Patil and U. J. Chavan, *Thin Solid Films*, 2016, **616**, 351–358.
172 S. Kumari, A. P. Singh, D. Sonal, R. Deva, S. Dass Shrivastav and V. R. Satsangi, *Int. J. Hydrogen Energy*, 2010, **35**, 3985–3990.
173 T. Ishihara, H. Kim, Y. Inoishi and J. Matsuda, *J. Am. Ceram. Soc.*, 2022, **105**, 6718–6731.
174 J. Suffner, S. Kaserer, H. Hahn, C. Roth and F. Ettingshausen, *Adv. Energy Mater.*, 2011, **1**, 648–654.
175 G. R. A. Kumara, C. S. K. Ranasinghe, E. N. Jayaweera, H. M. N. Bandara, M. Okuya and R. M. G. Rajapakse, *J. Phys. Chem. C*, 2014, **118**, 16479–16485.
176 E. L. Unger, F. Spadavecchia, K. Nonomura, P. Palmgren, G. Cappelletti, A. Hagfeldt, E. M. J. Johansson and G. Boschloo, *ACS Appl. Mater. Interfaces*, 2012, **4**, 5997–6004.
177 R. S. Ingole, B. Y. Fugare and B. J. Lokhande, *J. Mater. Sci.*, 2017, **28**, 16374–16383.
178 R. S. Ingole and B. J. Lokhande, *Mater. Lett.*, 2016, **168**, 95–98.
179 H. Xiu, T. Gao, N. An, Y. Wang, Y. Zhou, X. Qi, D. Liu and Y. Kuang, *ACS Appl. Energy Mater.*, 2022, **5**, 5127–5135.
180 S. F. Xue, Y. J. Li, F. H. Zheng, X. Bian, W. Y. Wu and C. H. Yang, *Rare Met.*, 2021, **40**, 31–39.
181 G. Scandura, P. Kumari, G. Palmisano, G. N. Karanikolos, J. Orwa and L. F. Dumée, *Ind. Eng. Chem. Res.*, 2023, **62**, 1736–1763.
182 Q. Zhang, H. Wu, S. Huang, X. Zhao, C. Hou, X. Zhuang, M. Wang, J. Han, Q. Chen and P. Liu, *ACS Appl. Energy Mater.*, 2023, **6**, 5435–5445.
183 S. L. Zhu, J. L. He, X. J. Yang, Z. D. Cui and L. L. Pi, *Electrochem. Commun.*, 2011, **13**, 250–253.
184 M. Niu, W. Xu, S. Zhu, Y. Liang, Z. Cui, X. Yang and A. Inoue, *J. Power Sources*, 2017, **362**, 10–19.
185 A. Stepanovich, K. Sliozberg, W. Schuhmann and A. Ludwig, *Int. J. Hydrogen Energy*, 2012, **37**, 11618–11624.
186 Z. Jin, J. Lyu, K. Hu, Z. Chen, G. Xie, X. Liu, X. Lin and H. J. Qiu, *Small*, 2021, **18**, 2107207.
187 K. Liang, X. Tang, B. Wei and W. Hu, *Mater. Res. Bull.*, 2013, **48**, 3829–3833.
188 M. Mirzaee and C. Dehghanian, *J. Solid State Electrochem.*, 2018, **22**, 3639–3645.
189 R. Li, N. Wu, J. Liu, Y. Jin, X. B. Chen and T. Zhang, *Corros. Sci.*, 2017, **119**, 23–32.
190 E. Hengge, J. Ihrenberger, E. M. Steyskal, R. Buzolin, M. Luckabauer, C. Sommitsch and R. Würschum, *Nanoscale Adv.*, 2023, **5**, 393–404.
191 S. H. Joo and H. Kato, *J. Alloys Compd.*, 2020, **831**, 154733.
192 R. Song, J. Han, M. Okugawa, R. Belosludov, T. Wada, J. Jiang, D. Wei, A. Kudo, Y. Tian, M. Chen and H. Kato, *Nat. Commun.*, 2022, **13**, 5157.
193 C. Zhao, T. Wada, V. De Andrade, G. J. Williams, J. Gelb, L. Li, J. Thieme, H. Kato and Y. C. K. Chen-Wiegart, *ACS Appl. Mater. Interfaces*, 2017, **9**, 34172–34184.
194 T. Wada, K. Yubuta and H. Kato, *Scr. Mater.*, 2016, **118**, 33–36.
195 C. Zhao, K. Kisslinger, X. Huang, J. Bai, X. Liu, C. H. Lin, L. C. Yu, M. Lu, X. Tong, H. Zhong, A. Pattammattel, H.

Yan, Y. Chu, S. Ghose, M. Liu and Y. C. K. Chen-Wiegart, *Nanoscale*, 2021, **13**, 17725–17736.
196 C. Zhao, K. Kisslinger, X. Huang, M. Lu, F. Camino, C. H. Lin, H. Yan, E. Nazaretski, Y. Chu, B. Ravel, M. Liu and Y. C. K. Chen-Wiegart, *Mater. Horiz.*, 2019, **6**, 1991–2002.
197 Y. Li, Q. Zhang, X. Zhao, H. Wu, X. Wang, Y. Zeng, Q. Chen, M. Chen and P. Liu, *Adv. Funct. Mater.*, 2023, **33**, 2214124.
198 Z. Lu, F. Zhang, D. Wei, J. Han, Y. Xia, J. Jiang, M. Zhong, A. Hirata, K. Watanabe, A. Karma, J. Erlebacher and M. Chen, *Acta Mater.*, 2021, **212**, 116916.
199 J. Han, C. Li, Z. Lu, H. Wang, Z. Wang, K. Watanabe and M. Chen, *Acta Mater.*, 2019, **163**, 161–172.
200 C. K. Chung, M. W. Liao, H. C. Chang and C. T. Lee, *Thin Solid Films*, 2011, **520**, 1554–1558.
201 Y. Li, N. Peng, Y. Wen and L. Liang, *Microporous Mesoporous Mater.*, 2020, **306**, 110412.
202 T. Dikici, M. Erol, M. Toparli and E. Celik, *Ceram. Int.*, 2014, **40**, 1587–1591.
203 J. Kapusta-Kołodziej, A. Chudecka and G. D. Sulka, *J. Electroanal. Chem.*, 2018, **823**, 221–233.
204 M. Erol, T. Dikici, M. Toparli and E. Celik, *J. Alloys Compd.*, 2014, **604**, 66–72.
205 L. Zaraska, D. Gilek, K. Gawlak, M. Jaskuła and G. D. Sulka, *Appl. Surf. Sci.*, 2016, **390**, 31–37.
206 D. V. Shinde, D. Y. Lee, S. A. Patil, I. Lim, S. S. Bhande, W. Lee, M. M. Sung, R. S. Mane, N. K. Shrestha and S. H. Han, *RSC Adv.*, 2013, **3**, 9431–9435.
207 T. Zhang, M. Paulose, R. Neupane, L. A. Schaffer, D. B. Rana, J. Su, L. Guo and O. K. Varghese, *Sol. Energy Mater. Sol. Cells*, 2020, **209**, 110472.
208 S. Xia, J. Ni, S. V. Savilov and L. Li, *Nano Energy*, 2018, **45**, 407–412.
209 H. Lee, V. S. Kumbhar, J. Lee, Y. Choi and K. Lee, *Electrochim. Acta*, 2020, **334**, 135618.
210 D. Lee, H. Lee, Y. T. Kim, K. Lee and J. Choi, *Electrochim. Acta*, 2020, **330**, 135192.
211 J. E. Yoo, J. Park, G. Cha and J. Choi, *Thin Solid Films*, 2013, **531**, 583–587.
212 K. S. Choudhari, C. H. Choi, S. Chidangil and S. D. George, *Nanomaterials*, 2022, **12**, 444.
213 P. Zhong, W. Que and X. Hu, *Appl. Surf. Sci.*, 2011, **257**, 9872–9878.
214 W. H. Baek, I. Seo, T. S. Yoon, H. H. Lee, C. M. Yun and Y. S. Kim, *Sol. Energy Mater. Sol. Cells*, 2009, **93**, 1587–1591.
215 V. M. Janardhanan, V. Heuveline and O. Deutschmann, *J. Power Sources*, 2008, **178**, 368–372.
216 X. Lu, T. M. M. Heenan, J. J. Bailey, T. Li, K. Li, D. J. L. Brett and P. R. Shearing, *J. Power Sources*, 2017, **365**, 210–219.
217 J. G. Rix, B. Mo, A. Y. Nikiforov, U. B. Pal, S. Gopalan and S. N. Basu, *J. Electrochem. Soc.*, 2021, **168**, 114507.
218 S. Ji, H. G. Seo, S. Lee, J. Seo, Y. Lee, W. H. Tanveer, S. W. Cha and W. Jung, *RSC Adv.*, 2017, **7**, 23600–23606.
219 K. J. Kim, B. H. Park, S. J. Kim, Y. Lee, H. Bae and G. M. Choi, *Sci. Rep.*, 2016, **6**, 22443.
220 M. Liu, D. Dong, R. Peng, J. Gao, J. Diwu, X. Liu and G. Meng, *J. Power Sources*, 2008, **180**, 215–220.
221 M. Singh, D. Zappa and E. Comini, *Mater. Adv.*, 2022, **3**, 5922–5929.
222 C. Jin, Y. Mao, N. Zhang and K. Sun, *Int. J. Hydrogen Energy*, 2015, **40**, 8433–8441.
223 M. Liu, D. Ding, Y. Bai, T. He and M. Liu, *J. Electrochem. Soc.*, 2012, **159**, B661–B665.
224 J. Liu, F. Yang, Z. Jiang, Y. Zhang, E. Hu, H. Wang and X. Yang, *ACS Appl. Energy Mater.*, 2021, **4**, 13492–13503.
225 H. Su, W. Zhang and Y. H. Hu, *Proc. Natl. Acad. Sci. U. S. A.*, 2022, **119**, e2208750119.
226 Y. Guo, M. Bessaa, S. Aguado, M. C. Steil, D. Rembelski, M. Rieu, J. P. Viricelle, N. Benameur, C. Guizard, C. Tardivat, P. Vernoux and D. Farrusseng, *Energy Environ. Sci.*, 2013, **6**, 2119–2123.
227 J. W. Yang, S. H. Ahn and H. W. Jang, *Curr. Opin. Green Sustainable Chem.*, 2021, **29**, 100454.
228 B. R. Lee, S. Choi, W. S. Cheon, J. W. Yang, M. G. Lee, S. H. Park and H. W. Jang, *Electron. Mater. Lett.*, 2022, **18**, 391–399.
229 M. G. Lee, J. W. Yang, H. R. Kwon and H. W. Jang, *CrystEngComm*, 2022, **24**, 5838–5864.
230 J. Park, T. H. Lee, C. Kim, S. A. Lee, M. J. Choi, H. Kim, J. W. Yang, J. Lim and H. W. Jang, *Appl. Catal., B*, 2021, **295**, 120276.
231 J. W. Yang, Y. J. Ahn, D. K. Cho, J. Y. Kim and H. W. Jang, *Inorg. Chem. Front.*, 2023, **10**, 3781–3807.
232 S. Bera, S. A. Lee, C. M. Kim, H. Khan, H. W. Jang and S. H. Kwon, *Chem. Mater.*, 2018, **30**, 8501–8509.
233 M. J. Choi, T. L. Kim, K. S. Choi, W. Sohn, T. H. Lee, S. A. Lee, H. Park, S. Y. Jeong, J. W. Yang, S. Lee and H. W. Jang, *ACS Appl. Mater. Interfaces*, 2022, **14**, 7788–7795.
234 J. W. Jang, C. Du, Y. Ye, Y. Lin, X. Yao, J. Thorne, E. Liu, G. McMahon, J. Zhu, A. Javey, J. Guo and D. Wang, *Nat. Commun.*, 2015, **6**, 7447.
235 Y. Fu, Y. R. Lu, F. Ren, Z. Xing, J. Chen, P. Guo, W. F. Pong, C. L. Dong, L. Zhao and S. Shen, *Sol. RRL*, 2020, **4**, 1900349.
236 Z. Zhang, I. Karimata, H. Nagashima, S. Muto, K. Ohara, K. Sugimoto and T. Tachikawa, *Nat. Commun.*, 2019, **10**, 4832.
237 K. Y. Yoon, J. Park, M. Jung, S. G. Ji, H. Lee, J. H. Seo, M. J. Kwak, S. Il Seok, J. H. Lee and J. H. Jang, *Nat. Commun.*, 2021, **12**, 4309.
238 H. Zhang, D. Li, W. J. Byun, X. Wang, T. J. Shin, H. Y. Jeong, H. Han, C. Li and J. S. Lee, *Nat. Commun.*, 2020, **11**, 4622.
239 K. H. Ye, H. Li, D. Huang, S. Xiao, W. Qiu, M. Li, Y. Hu, W. Mai, H. Ji and S. Yang, *Nat. Commun.*, 2019, **10**, 3687.
240 K. Zhang, B. Jin, C. Park, Y. Cho, X. Song, X. Shi, S. Zhang, W. Kim, H. Zeng and J. H. Park, *Nat. Commun.*, 2019, **10**, 2001.
241 K. J. McDonald and K. S. Choi, *Energy Environ. Sci.*, 2012, **5**, 8553–8557.
242 D. K. Lee and K. S. Choi, *Nat. Energy*, 2018, **3**, 53–60.

243 J. W. Yang, I. J. Park, S. A. Lee, M. G. Lee, T. H. Lee, H. Park, C. Kim, J. Park, J. Moon, J. Y. Kim and H. W. Jang, *Appl. Catal., B*, 2021, **293**, 120217.
244 M. G. Lee, D. H. Kim, W. Sohn, C. W. Moon, H. Park, S. Lee and H. W. Jang, *Nano Energy*, 2016, **28**, 250–260.
245 M. G. Lee, K. Jin, K. C. Kwon, W. Sohn, H. Park, K. S. Choi, Y. K. Go, H. Seo, J. S. Hong, K. T. Nam and H. W. Jang, *Adv. Sci.*, 2018, **5**, 1800727.
246 M. G. Lee, J. W. Yang, H. Park, C. W. Moon, D. M. Andoshe, J. Park, C. K. Moon, T. H. Lee, K. S. Choi, W. S. Cheon, J. J. Kim and H. W. Jang, *Nano-Micro Lett.*, 2022, **14**, 48.
247 M. G. Lee, J. W. Yang, I. J. Park, T. H. Lee, H. Park, W. S. Cheon, S. A. Lee, H. Lee, S. G. Ji, J. M. Suh, J. Moon, J. Y. Kim and H. W. Jang, *Carbon Energy*, 2023, **5**, e321.
248 S. Bera, S. A. Lee, W. J. Lee, J. H. Kim, C. Kim, H. G. Kim, H. Khan, S. Jana, H. W. Jang and S. H. Kwon, *ACS Appl. Mater. Interfaces*, 2021, **13**, 14291–14301.
249 A. Hagfeldt, G. Boschloo, L. Sun, L. Kloo and H. Pettersson, *Chem. Rev.*, 2010, **110**, 6595–6663.
250 D. Kishore Kumar, J. Kříž, N. Bennett, B. Chen, H. Upadhayaya, K. R. Reddy and V. Sadhu, *Mater. Sci. Energy Technol.*, 2020, **3**, 472–481.
251 M. Kokkonen, P. Talebi, J. Zhou, S. Asgari, S. A. Soomro, F. Elsehrawy, J. Halme, S. Ahmad, A. Hagfeldt and S. G. Hashmi, *J. Mater. Chem. A*, 2021, **9**, 10527–10545.
252 X. Hou, K. Aitola and P. D. Lund, *Energy Sci. Eng.*, 2021, **9**, 921–937.
253 B. D. Choudhury, C. Lin, S. M. A. Z. Shawon, J. Soliz-Martinez, H. Huq and M. J. Uddin, *Sci. Rep.*, 2021, **11**, 7552.
254 Y. Ding, L. Zhou, L. Mo, L. Jiang, L. Hu, Z. Li, S. Chen and S. Dai, *Adv. Funct. Mater.*, 2015, **25**, 5946–5953.
255 D. Chen, L. Cao, F. Huang, P. Imperial, Y. B. Cheng and R. A. Caruso, *J. Am. Chem. Soc.*, 2010, **132**, 4438–4444.
256 S. Yu, J. S. You, I. S. Yang, P. Kang, S. B. Rawal, S. Do Sung and W. I. Lee, *J. Power Sources*, 2016, **325**, 7–14.
257 S. Q. Kang, E. Z. Chen, J. Di Cheng, X. Y. Gu, K. Wei, G. Z. Sun, X. P. Gao, X. J. Pan, J. Y. Zhou and E. Q. Xie, *J. Alloys Compd.*, 2022, **905**, 164295.
258 A. Listorti, B. O'Regan and J. R. Durrant, *Chem. Mater.*, 2011, **23**, 3381–3399.
259 S. Il Cho, H. K. Sung, S. J. Lee, W. H. Kim, D. H. Kim and Y. S. Han, *Nanomaterials*, 2019, **9**, 1645.
260 J. Yue, Y. Xiao, Y. Li, G. Han, Y. Zhang and W. Hou, *Org. Electron.*, 2017, **43**, 121–129.
261 A. Banik, M. S. Ansari and M. Qureshi, *ACS Omega*, 2018, **3**, 14482–14493.
262 Q. Zhang, S. Hou and C. Li, *Nanomaterials*, 2020, **10**, 1598.
263 H. F. Etefa, V. Kumar, F. B. Dejene, M. T. Efa and L. T. Jule, *ACS Omega*, 2023, **8**, 15249–15258.
264 N. Li, E. A. Gibson, P. Qin, G. Boschloo, M. Gorlov, A. Hagfeldt and L. Sun, *Adv. Mater.*, 2010, **22**, 1759–1762.
265 M. Zannotti, E. Benazzi, L. A. Stevens, M. Minicucci, L. Bruce, C. E. Snape, E. A. Gibson and R. Giovannetti, *ACS Appl. Energy Mater.*, 2019, **2**, 7345–7353.
266 G. G. Wang, Z. Q. Lin, D. D. Zhao and J. C. Han, *Langmuir*, 2018, **34**, 8898–8903.
267 T. B. Tran, F. AlQatari and Q. H. Luc, *Sci. Rep.*, 2021, **11**, 4981.
268 S. Zhou, X. Zhao, P. Du, Z. Zhang, X. Liu, S. Liu and L. J. Guo, *Nanoscale*, 2022, **14**, 4887–4907.
269 H. Hu, B. Tang, H. Wan, H. Sun, S. Zhou, J. Dai, C. Chen, S. Liu and L. J. Guo, *Nano Energy*, 2020, **69**, 104427.
270 Y. C. Lee, S. C. Yeh, Y. Y. Chou, P. J. Tsai, J. W. Pan, H. M. Chou, C. H. Hou, Y. Y. Chang, M. S. Chu, C. H. Wu and C. H. Ho, *Microelectron. Eng.*, 2013, **105**, 86–90.
271 C. Y. Chou, W. H. Lai, X. F. Li, C. Cheng, C. K. Huang and C. Y. Liu, *Opt. Mater.*, 2021, **119**, 111297.
272 S. H. Chao, L. H. Yeh, R. T. Wu, K. Kawagishi and S. C. Hsu, *RSC Adv.*, 2020, **10**, 16284–16290.
273 Q. Zhou, M. Xu, Q. Li and H. Wang, *IEEE Photonics Technol. Lett.*, 2017, **29**, 983–986.
274 Y. Cheng, L. Wang, Y. Zhang, H. Zheng, J. Ma, X. Yi, G. Wang and J. Li, *ECS Solid State Lett.*, 2013, **2**, 93–97.
275 W. C. Ke, F. W. Lee, C. Y. Chiang, Z. Y. Liang, W. K. Chen and T. Y. Seong, *ACS Appl. Mater. Interfaces*, 2016, **8**, 34520–34529.
276 V. Wood, M. J. Panzer, J. E. Halpert, J. M. Caruge, M. G. Bawendi and V. Bulović, *ACS Nano*, 2009, **3**, 3581–3586.
277 W. S. Chen, S. H. Yang, W. C. Tseng, W. W. S. Chen and Y. C. Lu, *ACS Omega*, 2021, **6**, 13447–13455.
278 N. Kirkwood, B. Singh and P. Mulvaney, *Adv. Mater. Interfaces*, 2016, **3**, 1600868.
279 H.-C. Wang, S.-Y. Lin, A.-C. Tang, B. P. Singh, H.-C. Tong, C.-Y. Chen, Y.-C. Lee, T.-L. Tsai and R.-S. Liu, *Angew. Chem.*, 2016, **128**, 8056–8061.
280 J. K. Kim, S. Chhajed, M. F. Schubert, E. F. Schubert, A. J. Fischer, M. H. Crawford, J. Cho, H. Kim and C. Sone, *Adv. Mater.*, 2008, **20**, 801–804.
281 Y. An, Y. Tian, Q. Man, H. Shen, C. Liu, Y. Qian, S. Xiong, J. Feng and Y. Qian, *ACS Nano*, 2022, **16**, 6755–6770.
282 Z. Liu, X. Yuan, S. Zhang, J. Wang, Q. Huang, N. Yu, Y. Zhu, L. Fu, F. Wang, Y. Chen and Y. Wu, *NPG Asia Mater.*, 2019, **11**, 12.
283 D. Liu, Z. Yang, P. Wang, F. Li, D. Wang and D. He, *Nanoscale*, 2013, **5**, 1917–1921.
284 S. Liu, L. Kang and S. C. Jun, *Adv. Mater.*, 2021, **33**, 2004689.
285 Z. Li, Y. Tan, X. Huang, W. Zhang, Y. Gao and B. Tang, *Ceram. Int.*, 2016, **42**, 18887–18893.
286 M. Nagasaki and K. Kanamura, *ACS Appl. Energy Mater.*, 2019, **2**, 3896–3903.
287 G. Lui, G. Li, X. Wang, G. Jiang, E. Lin, M. Fowler, A. Yu and Z. Chen, *Nano Energy*, 2016, **24**, 72–77.
288 D. Tonti, M. J. Torralvo, E. Enciso, I. Sobrados and J. Sanz, *Chem. Mater.*, 2008, **20**, 4783–4790.
289 B. Qu, L. Hu, Q. Li, Y. Wang, L. Chen and T. Wang, *ACS Appl. Mater. Interfaces*, 2014, **6**, 731–736.
290 S. Lou, X. Cheng, Y. Zhao, A. Lushington, J. Gao, Q. Li, P. Zuo, B. Wang, Y. Gao, Y. Ma, C. Du, G. Yin and X. Sun, *Nano Energy*, 2017, **34**, 15–25.
291 J. Wang, H. Zhou, J. Nanda and P. V. Braun, *Chem. Mater.*, 2015, **27**, 2803–2811.

292 C. Liu, E. I. Gillette, X. Chen, A. J. Pearse, A. C. Kozen, M. A. Schroeder, K. E. Gregorczyk, S. B. Lee and G. W. Rubloff, *Nat. Nanotechnol.*, 2014, **9**, 1031–1039.
293 K. Dai, X. Wang, Y. Yin, C. Hao and Z. You, *Sci. Rep.*, 2016, **6**, 38794.
294 P. K. Panda, A. Grigoriev, Y. K. Mishra and R. Ahuja, *Nanoscale Adv.*, 2020, **2**, 70–108.
295 D. Nandi, V. B. Mohan, A. K. Bhowmick and D. Bhattacharyya, *J. Mater. Sci.*, 2020, **55**, 6375–6400.
296 S. Liu, Y. Yin, D. Ni, K. S. Hui, M. Ma, S. Park, K. N. Hui, C. Y. Ouyang and S. C. Jun, *Energy Storage Mater.*, 2019, **22**, 384–396.
297 S. Liu, L. Kang, J. Hu, E. Jung, J. Henzie, A. Alowasheeir, J. Zhang, L. Miao, Y. Yamauchi and S. C. Jun, *Small*, 2022, **18**, 2104507.
298 S. Liu, L. Kang, J. Zhang, E. Jung, S. Lee and S. C. Jun, *Energy Storage Mater.*, 2020, **32**, 167–177.
299 L. Kang, M. Zhang, J. Zhang, S. Liu, N. Zhang, W. Yao, Y. Ye, C. Luo, Z. Gong, C. Wang, X. Zhou, X. Wu and S. C. Jun, *J. Mater. Chem. A*, 2020, **8**, 24053–24064.
300 S. Liu, L. Kang, J. Hu, E. Jung, J. Zhang, S. C. Jun and Y. Yamauchi, *ACS Energy Lett.*, 2021, **6**, 3011–3019.
301 C. Xiong, T. Li, Y. Zhu, T. Zhao, A. Dang, H. Li, X. Ji, Y. Shang and M. Khan, *J. Alloys Compd.*, 2017, **695**, 1248–1259.
302 J. Kim, J. H. Eum, J. Kang, O. Kwon, H. Kim and D. W. Kim, *Sci. Rep.*, 2021, **11**, 2063.
303 S. K. Singh, V. M. Dhavale, R. Boukherroub, S. Kurungot and S. Szunerits, *Appl. Mater. Today*, 2017, **8**, 141–149.
304 D. Majumdar, T. Maiyalagan and Z. Jiang, *ChemElectroChem*, 2019, **6**, 4343–4372.
305 V. D. Patake and C. D. Lokhande, *Appl. Surf. Sci.*, 2008, **254**, 2820–2824.
306 R. Wang, Y. Ma, H. Wang, J. Key, D. Brett, S. Ji, S. Yin and P. K. Shen, *J. Mater. Chem. A*, 2016, **4**, 5390–5394.
307 J. Lee, J. Y. Seok, S. Son, M. Yang and B. Kang, *J. Mater. Chem. A*, 2017, **5**, 24585–24593.
308 A. Kumar, G. R. Dillip, A. Bharti, U. Maitra and A. J. Bhattacharyya, *Electrochem. Sci. Adv.*, 2021, **2**, e2100043.
309 J. Wang, X. Guo, R. Cui, H. Huang, B. Liu, Y. Li, D. Wang, D. Zhao, J. Dong, S. Li and B. Sun, *ACS Appl. Nano Mater.*, 2020, **3**, 11152–11159.
310 Y. Ding, S. Tang, R. Han, S. Zhang, G. Pan and X. Meng, *Sci. Rep.*, 2020, **10**, 11023.
311 G. H. Jeong, S. Baek, S. Lee and S. W. Kim, *Chem. – Asian J.*, 2016, **11**, 949–964.
312 B. Lesbayev, M. Auyelkhankyzy, G. Ustayeva, M. Yeleuov, N. Rakhymzhan, Y. Maral and A. Tolynbekov, *J. Compos. Sci.*, 2023, **7**, 20.
313 X. Lang, A. Hirata, T. Fujita and M. Chen, *Nat. Nanotechnol.*, 2011, **6**, 232–236.
314 H. Chen, S. Zhou and L. Wu, *ACS Appl. Mater. Interfaces*, 2014, **6**, 8621–8630.
315 R. R. Salunkhe, J. Tang, Y. Kamachi, T. Nakato, J. H. Kim and Y. Yamauchi, *ACS Nano*, 2015, **9**, 6288–6296.